

ENERGY CONSERVATION AND GRAVITY WAVES IN SOUND-PROOF TREATMENTS OF STELLAR INTERIORS: PART I ANELASTIC APPROXIMATIONS

BENJAMIN P. BROWN

Dept. Astronomy, University of Wisconsin, Madison, WI 53706-1582 and
 Center for Magnetic Self Organization in Laboratory and Astrophysical Plasmas, University of Wisconsin, 1150 University Avenue,
 Madison, WI 53706, USA

GEOFFREY M. VASIL

Canadian Institute for Theoretical Astrophysics, University of Toronto, 60 St. George Street, Toronto, ON M5S 3H8 Canada

ELLEN G. ZWEIBEL

Dept. Astronomy, University of Wisconsin, Madison, WI 53706-1582 and
 Center for Magnetic Self Organization in Laboratory and Astrophysical Plasmas, University of Wisconsin, 1150 University Avenue,
 Madison, WI 53706, USA

(Received Jan 26, 2012; Accepted Jul 10, 2012)
Accepted for publication in ApJ

ABSTRACT

Typical flows in stellar interiors are much slower than the speed of sound. To follow the slow evolution of subsonic motions, various sound-proof equations are in wide use, particularly in stellar astrophysical fluid dynamics. These low-Mach number equations include the anelastic equations. Generally, these equations are valid in nearly adiabatically stratified regions like stellar convection zones, but may not be valid in the sub-adiabatic, stably stratified stellar radiative interiors. Understanding the coupling between the convection zone and the radiative interior is a problem of crucial interest and may have strong implications for solar and stellar dynamo theories as the interface between the two, called the tachocline in the Sun, plays a crucial role in many solar dynamo theories. Here we study the properties of gravity waves in stably-stratified atmospheres. In particular, we explore how gravity waves are handled in various sound-proof equations. We find that some anelastic treatments fail to conserve energy in stably-stratified atmospheres, instead conserving pseudo-energies that depend on the stratification, and we demonstrate this numerically. One anelastic equation set does conserve energy in all atmospheres and we provide recommendations for converting low-Mach number anelastic codes to this set of equations.

Keywords: stars:interiors – Sun:interior

1. INTRODUCTION & MOTIVATION

In astrophysical fluid dynamics, the evolution time of the fluid flow is often substantially longer than the sound crossing time of the system. This is particularly true for convection deep in stellar interiors where the flows are very subsonic. Near the base of the solar convection zone the sound speed is about 220 km/s, while the convective velocities are likely of order hundreds of meters per second. Following the evolution of sound directly imposes crippling computational limits on simulations of such flows, as their evolution times are typically many convective turnover times, each of which is often several thousand sound times.

So called “sound-proof” equations address this separation of scales by beginning with the Navier-Stokes equations and filtering out fast, high-frequency sound waves while retaining compressible motions on slower time scales due to gravitational stratification. These motions include gravity waves in stably stratified regions and asymmetric convection in unstably stratified regions, with typically broad slow upflows and narrow fast downflows. In astrophysical and geophysical settings, the most commonly employed “sound-proof”

equations are the anelastic equations (Batchelor 1953; Ogura & Phillips 1962; Gough 1969). These have been employed in various astrophysical and geophysical codes to study solar convection and the solar dynamo (e.g., Gilman & Glatzmaier 1981; Glatzmaier 1984, 1985; Clune et al. 1999; Miesch et al. 2000; Elliott et al. 2000; Brun & Toomre 2002; Brun et al. 2004), stellar convection and dynamos (e.g., Browning et al. 2004; Brun et al. 2005; Brown et al. 2008, 2010, 2011; Nelson et al. 2011), the buoyant rise of magnetic structures (e.g., Lantz & Fan 1999), terrestrial convection and the geodynamo (e.g., Braginsky & Roberts 1995; Glatzmaier & Roberts 1996; Roberts & Glatzmaier 2000; Olson & Christensen 2006; Jones et al. 2009; Jones & Kuzanyan 2009) and the coupling of an unstably stratified convection zone to a stably stratified region beneath (e.g., Rogers et al. 2003; Rogers & Glatzmaier 2005b,a, 2006; Browning et al. 2006; Rogers et al. 2006, 2008; Rogers & MacGregor 2011; Brun et al. 2011). Recently a significant benchmarking effort has been undertaken to compare the various implementations of the anelastic equations (Jones et al. 2011).

Formally the anelastic approximation is only valid for an adiabatic or nearly adiabatic atmosphere. The solar convection zone is nearly adiabatic but it is underlain

by a stably stratified radiative zone; unsurprisingly the anelastic equations are often extended into this region where their validity may break down, to study the coupling of penetrative convection with a stably-stratified region (e.g., Rogers & Glatzmaier 2006; Rogers et al. 2008; Rogers & MacGregor 2010, 2011; Brun et al. 2011). This is particularly important in simulations of the solar dynamo, as the stably stratified internal boundary layer known as the tachocline at the base of the convection zone is thought to play a major role in the global-scale dynamo.

Fundamentally, the anelastic equations filter sound waves by modifying the continuity equation of the fully compressible Navier-Stokes equations. Questions about the energy conserving properties of the anelastic approximation have remained a thorny issue in the fluid dynamics community, with an especially vigorous debate occurring in the atmospheric sciences (e.g., Durran 1989; Bannon 1996), where these equations were originally derived. Likewise, there are several competing anelastic approaches, including “co-density” formulations (e.g., Lantz 1992; Braginsky & Roberts 1995, hereafter the LBR equations) and their different properties are unclear.

An alternate approach to sound-proofing the Navier-Stokes equations are the pseudo-incompressible equations, where the pressure rather than continuity equation is modified. These equations were proposed in (Durran 1989) and have recently been adopted in the astrophysical fluid dynamics community (e.g., Almgren et al. 2006a,b; Zingale et al. 2009) and see particular use in the MAESTRO code (Nonaka et al. 2010). The properties of gravity waves and stable-layer dynamics in the pseudo-incompressible equations have been explored extensively in the atmospheric sciences community, with several comparisons against the properties of the anelastic equations (Durran 1989, 2008; Nance & Durran 1994; Achatz et al. 2010; Klein et al. 2010). We reserve further discussion of gravity waves in this set of equations for a later paper.

Here we explore three implementations of the anelastic equations, one used in the anelastic spherical harmonic (ASH) code, and two different implementations of the “co-density” formulation (LBR equations). These equation sets are detailed in Section 2. We show that the anelastic equations based directly on the Navier-Stokes equations (anelastic Navier-Stokes, or ANS equations) behave incorrectly in stably stratified region. First we analytically study wave motions in an isothermal atmosphere in Section 3. We find that these equations do not conserve energy and instead conserve an entropy-weighted “pseudo-energy” (Section 4). We find however that the LBR equations do behave correctly for strongly stratified regions, conserving energy and reproducing the results obtained from the full compressible Euler equations. This is surprising, as the LBR equations make further assumptions of adiabaticity beyond those contained in the basic ANS equations, but these assumptions lie at the heart of the energy-conserving properties. As a consequence, adjustments to the LBR equations to more correctly capture the sub-adiabatic stratification can have profound consequences, introducing a completely different form of energy non-conservation (e.g., Rogers & Glatzmaier 2005b, and hereafter the RG

equations). We explore the behavior of these differing equations further in bounded atmospheres and spherical geometries in Section 5 and perform numerical simulations that show the difference between the normal ANS equations and the LBR equations. The implications of these findings for simulations of solar convection is discussed in Section 6, which also give suggestions for improving anelastic treatments of stably-stratified regions. The reader who is primarily interested in implementing energy-conserving anelastic equations should read Sections 2, 5 and 6.

2. MODEL EQUATIONS

2.1. Fully compressible Euler equations

For the purposes of this paper, the most general equations for fluid dynamics in the solar interior are the fully compressible Navier-Stokes equations. When viscosity is neglected, as we do here, these are known as the fully compressible Euler equations (FC equations). The equations of continuity and momentum are

$$\frac{\partial \rho}{\partial t} + \mathbf{u} \cdot \nabla \rho = -\rho \nabla \cdot \mathbf{u}, \quad (1)$$

$$\rho \left(\frac{\partial \mathbf{u}}{\partial t} + \mathbf{u} \cdot \nabla \mathbf{u} \right) = -\nabla P + \rho \mathbf{g}, \quad (2)$$

with gravitational acceleration $\mathbf{g} = -g\hat{\mathbf{r}}$. For an ideal gas,

$$P = \mathcal{R}\rho T = (\gamma - 1)\rho \mathcal{E}, \quad (3)$$

with \mathcal{E} the specific internal energy and $\gamma = c_P/c_V = 5/3$ is the ratio of specific heats. Here $c_P = \gamma/(\gamma - 1)\mathcal{R}$ is the specific heat at constant pressure. The evolution equations for temperature and pressure are

$$\frac{\partial T}{\partial t} + \mathbf{u} \cdot \nabla T = -(\gamma - 1)T \nabla \cdot \mathbf{u}, \quad (4)$$

$$\frac{\partial P}{\partial t} + \mathbf{u} \cdot \nabla P = -\gamma P \nabla \cdot \mathbf{u}, \quad (5)$$

where thermal conduction and other sources and sinks of energy are neglected.

Although equations (1–5) form a complete system, it will be useful during our discussion of the anelastic equations to rewrite these in terms of entropy S . Equations (4) and (5) can be combined with an equation of state linking the thermodynamic properties

$$\frac{dS}{c_P} = \frac{1}{\gamma} d \ln P - d \ln \rho = \frac{1}{\gamma} d \ln T - \frac{\gamma - 1}{\gamma} d \ln \rho \quad (6)$$

into an equation for the evolution of entropy fluctuations

$$\frac{\partial S}{\partial t} + \mathbf{u} \cdot \nabla S = 0. \quad (7)$$

We now specialize to the case of a hydrostatically balanced, stratified atmosphere with background density stratification ρ_0 , pressure P_0 , temperature T_0 and entropy S_0 that only vary with radius, with

$$\nabla P_0 = \rho_0 \mathbf{g}. \quad (8)$$

We define fluctuating quantities, denoted with subscript 1, by subtracting the time-independent hydrostatic atmosphere making no assumptions about relative amplitudes, with e.g., $P_1 \equiv P - P_0(r)$, thus these equations are fully nonlinear.

2.2. Anelastic models and fully compressible Euler equations in standard form

All anelastic approximations employ a continuity equation of the form

$$\nabla \cdot (\rho_0 \mathbf{u}) = 0. \quad (9)$$

Equation (9) derives from the assumption that the density fluctuations are small

$$\rho_1 \equiv \rho - \rho_0 \ll \rho_0. \quad (10)$$

In this case, the fluctuating density is given by the linearized equation of state,

$$\frac{\rho_1}{\rho_0} = \frac{1}{\gamma} \frac{P_1}{P_0} - \frac{S_1}{c_P} = \frac{P_1}{P_0} - \frac{T_1}{T_0}, \quad (11)$$

and though using a linear equation of state is not strictly required, we find it a clarifying simplification for the current discussion.

We consider equation (9) to be the defining characteristic of anelastic models. There exist however a variety of different treatments for the momentum and energy equations in the anelastic literature. In the following subsections we will consider three common formulations. The different notation and different thermodynamics used in the various anelastic treatments leads to some confusion. To remedy this, we reproduce each set of models under as consistent a notation as possible. Practical *numerical* or computational differences can arise when *solving* different transformations of the same fundamental model, but these issues lie beyond our current scope. Therefore, we consider two models identical if one can bring them into the same form by legitimate mathematical transformation, i.e., without approximation.

For comparison with the anelastic equations we first write the FC equations in standard form. With a linearized equation of state (11), we rewrite the buoyancy term involving pressure fluctuations in the following fashion

$$\frac{P_1}{\gamma P_0} \mathbf{g} = \frac{P_1}{\rho_0} \frac{\nabla P_0}{\gamma P_0} = \frac{P_1}{\rho_0} \left[\nabla \left(\frac{S_0}{c_P} \right) + \nabla \ln \rho_0 \right], \quad (12)$$

where we have used equations (8) and (6). We now introduce the reduced or kinematic pressure ϖ with

$$\varpi \equiv \frac{P_1}{\rho_0}. \quad (13)$$

The fully compressible Euler equations, with an entropy based energy equation and reduced pressure ϖ , are

$$\frac{\partial \rho_1}{\partial t} + \mathbf{u} \cdot \nabla \rho_0 = -\rho_0 \nabla \cdot \mathbf{u}, \quad (14)$$

$$\frac{\partial \mathbf{u}}{\partial t} + \mathbf{u} \cdot \nabla \mathbf{u} = -\nabla \varpi + \varpi \nabla \left(\frac{S_0}{c_P} \right) - \frac{S_1}{c_P} \mathbf{g}, \quad (15)$$

$$\frac{\partial S_1}{\partial t} + \mathbf{u} \cdot \nabla S_1 = -\mathbf{u} \cdot \nabla S_0. \quad (16)$$

These equations linearize the thermodynamic variables (eq. 11) but are nonlinear in the velocities and are the counterparts of the anelastic equations that we now turn to; we do not solve these equations (14–16) but include them for illustrative purposes.

2.3. ANS Anelastic equations

In many anelastic equations the momentum equation is the same as in the FC equations (e.g., Gilman & Glatzmaier 1981; Drew et al. 1995;

Clune et al. 1999; Brun et al. 2004). We thus refer to these equations as the anelastic Navier-Stokes (ANS) equations. In the ANS equations, the momentum equation is

$$\rho_0 \left(\frac{\partial \mathbf{u}}{\partial t} + (\mathbf{u} \cdot \nabla) \mathbf{u} \right) = -\nabla P_1 + \rho_1 \mathbf{g}, \quad (17)$$

which with equation (11) can be transformed into the same form as equation (15), with

$$\frac{\partial \mathbf{u}}{\partial t} + \mathbf{u} \cdot \nabla \mathbf{u} = -\nabla \varpi + \varpi \nabla \left(\frac{S_0}{c_P} \right) - \frac{S_1}{c_P} \mathbf{g}. \quad (18)$$

The ANS momentum equation (18) can be written in an alternative form by combining ϖ terms to yield

$$\frac{\partial \mathbf{u}}{\partial t} + \mathbf{u} \cdot \nabla \mathbf{u} = -e^{(S_0/c_P)} \nabla \left(\varpi e^{-(S_0/c_P)} \right) - \frac{S_1}{c_P} \mathbf{g}, \quad (19)$$

which will be useful for our analysis in Section 4. As a notational issue, the stratification term interacting with ϖ in equation (19) takes the same form as a potential temperature, as is traditionally used in studies of geophysical flows in the atmosphere and ocean with

$$\Theta_0 \equiv e^{(S_0/c_P)} = \frac{P_0^{1/\gamma}}{\rho_0} \quad (20)$$

and, with the linearized equation of state (11),

$$\frac{\Theta_1}{\Theta_0} = \frac{S_1}{c_P}. \quad (21)$$

In terms of Θ , the ANS momentum equation is

$$\frac{\partial \mathbf{u}}{\partial t} + \mathbf{u} \cdot \nabla \mathbf{u} = -\Theta_0 \nabla (\varpi \Theta_0^{-1}) - \frac{\Theta_1}{\Theta_0} \mathbf{g}. \quad (22)$$

Neglecting diffusion and sources of energy, the energy equation is the same as in the FC equations (eq. 7), with a background entropy gradient

$$\frac{\partial S_1}{\partial t} + \mathbf{u} \cdot \nabla S_1 = -\mathbf{u} \cdot \nabla S_0. \quad (23)$$

Combined with the anelastic continuity equation (9), equations (18) and (23) constitute a full set of equations for anelastic motions.

2.4. LBR Anelastic equations

In the “co-density” equations or Lantz-Braginsky-Roberts equations (e.g., Lantz 1992; Braginsky & Roberts 1995; Lantz & Fan 1999; Jones et al. 2009, and hereafter LBR equations), the $\varpi \nabla (S_0/c_P)$ term is dropped and the momentum equation becomes

$$\frac{\partial \mathbf{u}}{\partial t} + \mathbf{u} \cdot \nabla \mathbf{u} = -\nabla \varpi - \frac{S_1}{c_P} \mathbf{g}, \quad (24)$$

or, in terms of potential temperatures,

$$\frac{\partial \mathbf{u}}{\partial t} + \mathbf{u} \cdot \nabla \mathbf{u} = \nabla \varpi - \frac{\Theta_1}{\Theta_0} \mathbf{g}. \quad (25)$$

As in the ANS equations, the energy equation (23) and the continuity equation (9) complete the full set of equations.

The LBR momentum equation (24) is derived from the full Euler momentum equation (2) by assuming $\nabla S_0 \approx 0$, as for a nearly adiabatic state. Despite this assumption, we find that the LBR equations perform well when $\nabla S_0 \neq 0$ while the ANS equations perform poorly in that same limit. Though Lantz (1992) and Braginsky & Roberts (1995) are typically credited

with independently deriving the LBR equations, these equations bear striking similarities to the Lipps-Hemler anelastic equations (Lipps & Hemler 1982, 1985; Lipps 1990), who were possibly the first to recognize the importance of introducing a reduced pressure and neglecting the interactions between fluctuating pressure and stratification. They likewise recognized that gravity waves derived from their anelastic equations conserved energy.

2.5. *RG anelastic equations*

Rogers & Glatzmaier (2005b) use a different set of anelastic equations (hereafter the RG equations). As above, neglecting viscosity and sources of heat, their equations are the momentum equation and a temperature based energy equation

$$\frac{\partial \mathbf{u}}{\partial t} + \mathbf{u} \cdot \nabla \mathbf{u} = -\nabla \varpi + \varpi \nabla \ln T_0 - \frac{T_1}{T_0} \mathbf{g}, \quad (26)$$

$$\frac{\partial T_1}{\partial t} + \mathbf{u} \cdot \nabla T_1 = -\mathbf{u} \cdot \nabla T_0 - (\gamma - 1)(T_0 + T_1) \nabla \cdot \mathbf{u}. \quad (27)$$

With the anelastic continuity equation (9), these constitute a full set of equations for anelastic motions.

Equation (26) can be equivalently written

$$\frac{\partial \mathbf{u}}{\partial t} + \mathbf{u} \cdot \nabla \mathbf{u} = -T_0 \nabla (\varpi/T_0) - \frac{T_1}{T_0} \mathbf{g}, \quad (28)$$

a form that will be useful in Section 4. By combining the equation of state (6) with the anelastic continuity equation (9), we can cast the energy equation in terms of entropy with

$$\left(\frac{\partial}{\partial t} + \mathbf{u} \cdot \nabla \right) \frac{T_1}{T_0} = -\gamma \left(1 + \frac{T_1}{T_0} \right) \mathbf{u} \cdot \nabla (S_0/c_P). \quad (29)$$

With a linearized equation of state, this takes the same form as the entropy equation (16), but with an extra factor of γ multiplying the background entropy gradient.

The right hand sides of the momentum equations for these four systems of equations are summarized in Table 1.

3. LINEAR WAVES IN AN ISOTHERMAL ATMOSPHERE

A plane-parallel isothermal atmosphere gives an analytically tractable background for computing eigenfrequencies and modes for linear gravity and/or acoustic waves. Computing these simple solutions helps elucidate the differences between the various anelastic treatments. Defining the velocity in terms of the vector displacement,

$$\mathbf{u} = \frac{\partial \boldsymbol{\xi}}{\partial t} \quad (30)$$

allows simple integration of the linear thermodynamic equations,

$$\rho_1/\rho_0 = -\boldsymbol{\xi} \cdot \nabla \ln \rho_0 - \nabla \cdot \boldsymbol{\xi}, \quad (31)$$

$$P_1/\gamma P_0 = -\boldsymbol{\xi} \cdot \nabla \ln P_0^{1/\gamma} - \nabla \cdot \boldsymbol{\xi}, \quad (32)$$

$$S_1 = -\boldsymbol{\xi} \cdot \nabla S_0. \quad (33)$$

For wavelike perturbations in an atmosphere of infinite extent, we can assume without loss of generality that

$$(\boldsymbol{\xi}, \rho_1, P_1, S_1) \propto f(Kr) \exp(i\omega t - imx) \quad (34)$$

where x is the horizontal coordinate, m is the horizontal wave number, and the vertical dependence on r has been left in general form with wavenumber K .

Table 1
Systems of equations

System	RHS momentum equation	eq
FC	$-\nabla \varpi + \varpi \nabla (S_0/c_P) - (S_1/c_P) \mathbf{g}$	(15)
ANS	$-\nabla \varpi + \varpi \nabla (S_0/c_P) - (S_1/c_P) \mathbf{g}$	(18)
LBR	$-\nabla \varpi - (S_1/c_P) \mathbf{g}$	(24)
RG	$-\nabla \varpi + \varpi \nabla \ln T_0 - (T_1/T_0) \mathbf{g}$	(26)
RHS wave momentum		
FC	$-\nabla \varpi + \varpi \nabla (S_0/c_P) + (\boldsymbol{\xi} \cdot \nabla)(S_0/c_P) \mathbf{g}$	
ANS	$-\nabla \varpi + \varpi \nabla (S_0/c_P) + (\boldsymbol{\xi} \cdot \nabla)(S_0/c_P) \mathbf{g}$	
LBR	$-\nabla \varpi + (\boldsymbol{\xi} \cdot \nabla)(S_0/c_P) \mathbf{g}$	
RG	$-\nabla \varpi + \varpi \nabla \ln T_0 + \gamma (\boldsymbol{\xi} \cdot \nabla)(S_0/c_P) \mathbf{g}$	
RHS momentum (for Section 4)		
ANS	$-e^{S_0/c_P} \nabla (\varpi e^{-S_0/c_P}) - (S_1/c_P) \mathbf{g}$	(18)
LBR	$-\nabla \varpi - (S_1/c_P) \mathbf{g}$	(24)
RG	$-T_0 \nabla (\varpi/T_0) - (T_1/T_0) \mathbf{g}$	(26)

Note. — In all systems of equations, $\varpi = P_1/\rho_0$. The fully compressible equations use continuity equation (1) while anelastic systems use equation (9). In the wave momentum equations, $\boldsymbol{\xi}$ is the displacement vector as defined in eq 30.

In a hydrostatically balanced isothermal atmosphere

$$\nabla_r \ln P_0 = \nabla_r \ln \rho_0 = -\frac{g}{\mathcal{R}T_0} = -\frac{1}{H} = -\frac{\gamma g}{c_S^2} \quad (35)$$

where H is the pressure or density scale height, ∇_r is the vertical derivative, and

$$c_S^2 \equiv \frac{\gamma P_0}{\rho_0} \quad (36)$$

is the (constant) sound speed. The Brunt-Väisälä frequency N is

$$N^2 \equiv -\mathbf{g} \cdot \nabla \left(\frac{S_0}{c_P} \right) = \frac{(\gamma - 1) g}{\gamma H}. \quad (37)$$

3.1. *Fully compressible equations*

The solution for the fully compressible equations is well known and can be found in several textbooks (e.g., Lighthill 1978). We begin with the linearized momentum equation for waves

$$-\rho_0 \omega^2 \boldsymbol{\xi} = -\nabla P_1 + \rho_1 \mathbf{g}, \quad (38)$$

and solve for eigenfrequencies using equations (30)–(32) and (34). Taking the vertical eigenfunction $f(Kr) = \exp(-iKr)$, the dispersion relationship for waves in an isothermally-stratified atmosphere is

$$-\frac{\omega^4}{c_S^2} + \omega^2 [K^2 + m^2 - iKH^{-1}] = m^2 N^2. \quad (39)$$

It is well known that the fully compressible Euler equations conserve energy. Their frequencies ω must thus be purely real with no imaginary component (see Section 4), yet equation (39) has an imaginary component. Taking a complex vertical wavenumber

$$K = k + i \frac{1}{2H} \quad (40)$$

with real component k resolves this. The vertical eigenfunction follows

$$f(Kr) = \exp(-iKr) = \exp\left(\frac{r}{2H}\right) \exp(-ikr). \quad (41)$$

All waves in this atmosphere share the properties that their eigenfunctions grow with height, their momentum density decreases with height

$$\rho_0 u \propto \exp\left(-\frac{r}{2H}\right), \quad (42)$$

while their kinetic energy $\rho_0 u^2$ is constant with height. These eigenfunctions are orthogonal with respect to the density weight

$$\int \rho_0 f(Kr) f(K'r)^* dr = \delta(k - k'), \quad (43)$$

with δ here the Dirac delta.

The final dispersion relationship with ω^2 real is

$$-\frac{\omega^4}{c_S^2} + \omega^2 \left[k^2 + m^2 + \frac{1}{4H^2} \right] = m^2 N^2. \quad (44)$$

with N^2 given by equation (37). The quadratic nature of equation (44) in ω^2 provides for two distinct branches of acoustic and gravity waves. In the high frequency limit $\omega^2 \gg N^2$,

$$\omega_{SW}^2 = \left[k^2 + m^2 + \frac{1}{4H^2} \right] c_S^2, \quad (45)$$

representing the propagation of pure sound waves in an atmosphere with an acoustic cutoff frequency $c_S^2/4H^2$. In the low frequency limit, we obtain pure internal gravity waves with

$$\omega_{GW}^2 = \frac{m^2}{k^2 + m^2 + \frac{1}{4H^2}} N^2. \quad (46)$$

The full solution for ω^2 follows

$$\omega^2 = \frac{\omega_{SW}^2}{2} \left(1 \pm \sqrt{1 - \frac{4\omega_{GW}^2}{\omega_{SW}^2}} \right) \quad (47)$$

with the positive root corresponding to the sound waves while the negative root corresponds to the internal gravity waves.

3.2. ANS gravity waves

We begin our analysis of the anelastic systems with the ANS equations. For linear waves, the continuity, momentum and energy equations are

$$\nabla \cdot \boldsymbol{\xi} = -\boldsymbol{\xi} \cdot \nabla \ln \rho_0, \quad (48)$$

$$-\omega^2 \boldsymbol{\xi} = -\nabla \varpi + \varpi \nabla \left(\frac{S_0}{c_P} \right) - \frac{S_1}{c_P} \mathbf{g}, \quad (49)$$

$$S_1 = -\boldsymbol{\xi} \cdot \nabla S_0. \quad (50)$$

Combining the vertical momentum equation (49) and the energy equation (50) for linearized waves, we obtain

$$\omega^2 \xi_r - \nabla_r(\varpi) + \varpi \nabla_r(S_0/c_P) = N^2 \xi_r, \quad (51)$$

where we have also used equation (37). We obtain ϖ by taking the horizontal divergence of the momentum equation

$$\omega^2 \nabla_{\perp} \cdot \boldsymbol{\xi} = \nabla_{\perp}^2 \varpi. \quad (52)$$

The dispersion relationship for linear waves is

$$\omega^2 \left[m^2 + \left(K - i \frac{2\gamma - 1}{2\gamma H} \right)^2 + \frac{1}{4\gamma^2 H^2} \right] = m^2 N^2. \quad (53)$$

Once again, ω^2 has an imaginary component. As with the fully compressible equations, we can try to absorb this imaginary component within the vertical eigenfunction, which leads to a vertical wave number

$$K = k + i \frac{1}{2H} \frac{2\gamma - 1}{\gamma}, \quad (54)$$

and vertical eigenfunction

$$f(Kr) = \exp(-iKr) = \exp\left(\frac{r}{2H} \frac{2\gamma - 1}{\gamma}\right) \exp(-ikr), \quad (55)$$

with time dependence

$$\omega_{ANS}^2 \left[m^2 + k^2 + \frac{1}{4\gamma^2 H^2} \right] = m^2 N^2. \quad (56)$$

A serious problem lurks within these choices however, as the momentum and kinetic energy densities scale as

$$\rho_0 u \propto \exp\left(-\frac{1}{2\gamma} \frac{r}{H}\right), \quad (57)$$

$$\rho_0 u^2 \propto \exp\left(\frac{\gamma - 1}{\gamma} \frac{r}{H}\right). \quad (58)$$

For adiabatic motions in an ideal gas, $\gamma = 5/3$, and the kinetic energy of the waves grows exponentially with height.

Alternatively, we can use the eigenfunctions from the fully compressible equations, in equations (41-40), which leads to the correct far-field behavior for momentum and energy, but leads to a dispersion relationship of

$$\omega_{ANS-I}^2 \left[m^2 + k^2 + \frac{1}{4H^2} \frac{2 - \gamma}{\gamma} + ikg(\gamma - 1) \right] = m^2 N^2. \quad (59)$$

There is now an imaginary component to ω^2 and anelastic gravity waves in an infinite isothermal atmosphere can have spurious growing (or decaying) modes. As we will see in Section 4, this bizarre behavior reflects the fact that the ANS equations do not conserve energy. Further, as we will see in Sections 4-5, the fact that these spurious modes have not been detected in simulations previously is likely related to the presence of a conserved pseudo-energy (i.e., a differently weighted quadratic integral of the fluctuating velocities and entropies).

3.3. LBR gravity waves

Finding linear eigenfrequencies in the LBR equations amounts to the same procedure as in Section 3.2. Now however the $\varpi \nabla(S_0/c_P)$ term is missing from the vertical momentum equation, and equation (51) becomes

$$\omega^2 \xi_r - \nabla_r \varpi = N^2 \xi_r. \quad (60)$$

This readily yields the following dispersion relationship

$$\omega^2 \left[m^2 + \left(K - i \frac{1}{2H} \right)^2 + \frac{1}{4H^2} \right] = m^2 N^2, \quad (61)$$

Requiring that $K = k + i/2H$ is clearly the natural choice for obtaining real frequencies. By employing the vertical

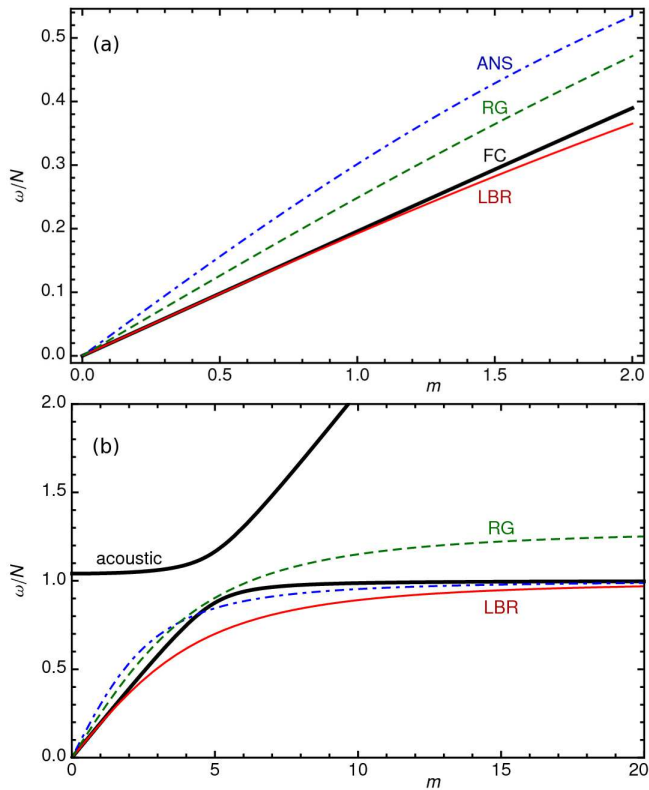


Figure 1. Dispersion relationships for gravity waves in an isothermal atmosphere of infinite extent with $1/H = 10$, for the fundamental mode $k = 1$ and with horizontal wavenumber m . (a) Frequencies for each set of equations in the low frequency limit ($\omega^2/N^2 \ll 1$). Shown are the gravity wave branch of the exact solutions for the fully compressible Euler equations (black, labelled FC, and given by eq 47). Also shown are the dispersion relation for the ANS equations (blue, dot-dashed), the LBR equations (red, solid), and the RG equations (green, dashed) with each line labeled. In this regime the LBR equations and exact solutions to the Euler (FC) equations are in good agreement, while the ANS and RG equations obtain frequencies that are too high. The corresponding dispersion relationships are given in Table 2. (b) Full frequency domain. At large m the ANS, LBR and FC equations converge to the Brunt-Väisälä frequency N , while the RG equations are too large by a factor of $\sqrt{\gamma}$. Here we also show the sound wave branch (black, labelled “acoustic”, and given by eq 47) of the exact solution to the full Euler equations.

eigenfunctions in equations (41-40) we get

$$\omega_{\text{LBR}}^2 \left[m^2 + k^2 + \frac{1}{4H^2} \right] = m^2 N^2, \quad (62)$$

which is the same as equation (46). Adiabatically propagating gravity waves solved with the LBR equations in an infinite isothermal atmosphere behave like the low frequency branch of the fully compressible equations in both their time dependence and their vertical structure.

3.4. RG gravity waves

Next we look at the propagation of gravity waves within the RG equations. In an isothermal atmosphere the coupling between ϖ and the background stratification disappears. With the anelastic continuity equa-

tion (48), the linear RG wave equations are

$$-\omega^2 \xi = -\nabla \varpi - \frac{T_1}{T_0} \mathbf{g}, \quad (63)$$

$$\frac{T_1}{T_0} = -\gamma \xi \cdot \nabla (S_0/c_P). \quad (64)$$

Combining the vertical momentum and energy equations yields

$$\omega^2 \xi_r - \nabla_r \varpi = \gamma N^2 \xi_r \quad (65)$$

This leads to a dispersion relationship of

$$\omega^2 \left[m^2 + \left(K - i \frac{1}{2H} \right)^2 + \frac{1}{4H^2} \right] = \gamma m^2 N^2. \quad (66)$$

As previously, the vertical eigenfunctions in equations (41-40) are the clear choice and lead to a final dispersion relationship of

$$\omega_{\text{RG}}^2 \left[m^2 + k^2 + \frac{1}{4H^2} \right] = m^2 \gamma N^2, \quad (67)$$

which is the same as equation (46) except for the factor of γ multiplying N^2 .

While the functional form of the frequencies given in equation (67) are correct up to a factor of $\sqrt{\gamma} \approx 1.29$ for $\gamma = 5/3$, and while the vertical structure of the eigenfunction matches with the fully compressible case, we note that this is a special case brought about by $\nabla \ln T_0 = 0$ in an isothermal atmosphere. In more general atmospheres, an extra term would exist in equation (63) of the form $\varpi \nabla \ln T_0$ and we would be faced by the same problems with energy conservation and growth that we found in Section 3.2 for the ANS equations. We will see this in Section 4.2.

We summarize the properties of gravity waves for all four systems of equations in an isothermal atmosphere of infinite extent in Table 2 and plot them for waves with $kH = 1/10$ in Figure 1. In the low-frequency regime (Figure 1a), the gravity wave branch of the exact solutions to the Euler equations (labelled FC, and given by eq 47) matches the dispersion relationship of the LBR equations closely, while the frequencies of gravity waves in the ANS and RG equations are too large. As the horizontal wavenumber m increases, the LBR dispersion relationship begins to diverge from the exact results. At still larger wavenumber m , both the ANS and LBR dispersion relationships return to agreement with the exact Euler solutions (Figure 1b). At all wavenumbers, the frequencies from the RG equations are a factor of $\sqrt{\gamma}$ larger than those obtained from the LBR equations and thus exceed the Brunt-Väisälä frequency N at large m . Higher order radial modes show similar behavior, though the relative differences between the LBR and FC dispersion relationships decreases as k increases.

4. CONSERVATION OF ENERGY AND PSEUDO-ENERGY

An important theme of this paper revolves around energy budgets in different approximations to the full Euler equations. The curious discrepancies found in isothermal atmospheres in Section 3 hint at deeper issues in these approximated equation sets. In this section, we find that those issues are associated with energy conservation and its violation. Here we consider general atmospheres, with

Table 2
Infinite isothermal atmosphere

System	$\omega^2 =$	eq
FC	$\left[m^2 + k^2 + \frac{1}{4H^2}\right]^{-1} m^2 N^2$	(46)
ANS	$\left[m^2 + k^2 + \frac{1}{4\gamma^2 H^2}\right]^{-1} m^2 N^2$	(56)
ANS-I	$\left[m^2 + k^2 + \frac{1}{4H^2} \frac{2-\gamma}{\gamma} + ikg(\gamma-1)\right]^{-1} m^2 N^2$	(59)
LBR	$\left[m^2 + k^2 + \frac{1}{4H^2}\right]^{-1} m^2 N^2$	(62)
RG	$\left[m^2 + k^2 + \frac{1}{4H^2}\right]^{-1} m^2 \gamma N^2$	(67)

Note. — Horizontal wavenumbers m and vertical wave numbers k are real quantities. In all systems of equations except ANS, we have taken the radial eigenfunctions corresponding to equations (41–40) which remain finite in the far-field limit. In the ANS equations, we instead take eigenfunctions (54–55), which leads to real ω but divergent behavior in the far-field limit. For the FC equations we here show only $\omega_{c_W}^2$ (the low-frequency limit); the full Euler dispersion relationship is given in equation (47).

Table 3
Energies and pseudo-energies

System	weight	eq	IA	RZ	CZ
FC	ρ_0	(75)	Y	Y	Y
ANS	$\exp(-S_0/c_p)\rho_0$	(88)	N	N	Y
LBR	ρ_0	(96)	Y	Y	Y
RG	$T_0^{-1}\rho_0$	(101)	Y	N	N

Note. — Weight required for self-adjointness and hence energy or pseudo-energy conservation in each system of equations, with reference to where the conservation properties are shown in the text. Systems with weights other than ρ_0 will not always conserve energy. Included are qualitative estimates of whether each set of equations is likely to conserve energy in an isothermal atmosphere (IA), in the stably stratified solar radiative zone (RZ), and in the nearly adiabatically stratified solar convection zone (CZ).

the isothermal atmospheres of Section 3 being a subset of these results. For each set of equations, beginning with the full Euler equations and proceeding with each anelastic equation set in turn, we derive the energy conservation properties for arbitrary nonlinear motions. We then consider the energy conserving properties of linearized motions including wave-like perturbations. We find that some equation sets (FC and LBR) conserve energy and behave as expected. We find that the other anelastic equation sets (ANS and RG) do not conserve energy and instead conserve a stratification-weighted pseudo-energy, which leads to some surprising and paradoxical results for wave-like motions. The key results of this section are summarized in Table 3.

4.1. Euler Energy Balance

We begin by considering the Euler equations. The main results of this subsection are well known in the literature (e.g., Lighthill 1978). Namely, in the fully compressible Euler equations, energy is conserved by wavelike motions and the temporal frequencies ω are purely real. However, for the purposes of comparison with anelastic models, we note that the fully nonlinear equations (1)–

(7) contain a statement of conservation of energy. Contracting equation (2) with velocity \mathbf{u} and assuming that gravity is given by a potential function gives

$$\frac{\partial E}{\partial t} + \nabla \cdot [\mathbf{u}(E + P)] = 0, \quad (68)$$

where

$$E = \frac{\rho|\mathbf{u}|^2}{2} + \frac{P}{\gamma-1} + \rho\Phi, \quad (69)$$

$$\mathbf{g} = -\nabla\Phi, \quad (70)$$

with Φ the gravitational potential. The fully compressible Euler equations conserve energy for arbitrary (non-linear) motions.

For the linearized version of the Euler equations, we may go a step further. For a system in hydrostatic balance (eq. 8), we write equation (38) in terms perturbed pressure P_1 and entropy S_1 as

$$\rho_0 \frac{\partial^2 \boldsymbol{\xi}}{\partial t^2} = -\nabla P_1 + \frac{P_1}{\gamma P_0} \nabla P_0 + \frac{g^2 \rho_0}{N^2} \frac{S_1}{c_p} \frac{\nabla S_0}{c_p}. \quad (71)$$

We introduce an arbitrary vector $\boldsymbol{\xi}'$ that is related to the displacement vector $\boldsymbol{\xi}$ (eq 30) and guided by equations (32) and (33) define P'_1 and S'_1 as

$$P'_1 = -\boldsymbol{\xi}' \cdot \nabla P_0 - \gamma P_0 \nabla \cdot \boldsymbol{\xi}', \quad (72)$$

$$S'_1 = -\boldsymbol{\xi}' \cdot \nabla S_0. \quad (73)$$

Contracting equation (71) with arbitrary $\boldsymbol{\xi}'$ and using equations (72) and (73) gives

$$\rho_0 \boldsymbol{\xi}' \cdot \frac{\partial^2 \boldsymbol{\xi}}{\partial t^2} + \frac{P_1}{\gamma P_0} P'_1 + \frac{g^2 \rho_0}{N^2} \frac{S_1}{c_p} \frac{S'_1}{c_p} + \nabla \cdot (\boldsymbol{\xi}' P_1) = 0. \quad (74)$$

We may derive a number of different results from equation (74). First we consider velocity perturbations and take $\boldsymbol{\xi}' = \partial_t \boldsymbol{\xi} = \mathbf{u}$ (thus $S'_1 = \partial_t S_1$ and $P'_1 = \partial_t P_1$). This choice gives the local conservation of energy for linear perturbations

$$\frac{\partial}{\partial t} \left(\frac{\rho_0 |\mathbf{u}|^2}{2} + \frac{g^2 \rho_0}{2N^2} \left(\frac{S_1}{c_p} \right)^2 + \frac{P_1^2}{2\gamma P_0} \right) + \nabla \cdot (\mathbf{u} P_1) = 0. \quad (75)$$

Integrating equation (75) over a volume V with $(\mathbf{u} \cdot \hat{\mathbf{n}}) P_1 = 0$ on the boundary ∂V , gives

$$\frac{\partial}{\partial t} (K + U) = 0, \quad (76)$$

where the kinetic and potential energies are given respectively by

$$K = \frac{1}{2} \int_V \rho_0 |\mathbf{u}|^2 d^3 \mathbf{x}, \quad (77)$$

$$U = \frac{1}{2} \int_V \left(\frac{g^2 \rho_0}{N^2} \left(\frac{S_1}{c_p} \right)^2 + \frac{P_1^2}{\gamma P_0} \right) d^3 \mathbf{x}. \quad (78)$$

Linear perturbations also conserve energy in the fully compressible Euler equations.

Choosing instead that $\boldsymbol{\xi}' = \boldsymbol{\xi}$ (with this choice, $S'_1 = S_1$ and $P'_1 = P_1$) in equation (74), integrating over volume V with $(\mathbf{u} \cdot \hat{\mathbf{n}}) P_1 = 0$ on boundary ∂V , and averaging over time gives a version of energy equipartition for linear perturbations, where the time average of the kinetic energy equals the time average of the potential energy.

Rather than considering energy conservation, we now consider the time-dependence of linearized displacements

$$\boldsymbol{\xi} = \hat{\boldsymbol{\xi}} e^{i\omega t}, \quad \boldsymbol{\xi}' = \hat{\boldsymbol{\xi}}^* e^{-i\omega t}, \quad (79)$$

where $\hat{\boldsymbol{\xi}}^*$ represents the complex conjugate of displacement $\hat{\boldsymbol{\xi}}$. Here, S'_1 gives the characteristic entropy perturbation S_1 associated with a displacement of amplitude $\hat{\boldsymbol{\xi}}$ and likewise with P'_1 and pressure perturbation P_1 . Integrating over the same volume, V , gives

$$\omega^2 \int_V \rho_0 |\boldsymbol{\xi}|^2 d^3 \mathbf{x} - \int_V \left(\frac{g^2 \rho_0 |S_1|^2}{N^2 c_p^2} + \frac{|P_1|^2}{\gamma P_0} \right) d^3 \mathbf{x} = 0. \quad (80)$$

All of the integrals in equation (80) are strictly real and positive definite, which implies that the squared temporal frequencies must also be real

$$\Im(\omega^2) = 0. \quad (81)$$

Equation (81) states that while instability may or may not exist, the system must transition from purely oscillating ($N^2 > 0$) to purely growing behavior ($N^2 < 0$). Neither growing nor damped waves exist in the fully compressible Euler equations.

Lastly, one may show that displacements with different frequencies are orthogonal with respect to the energy inner product,

$$\langle \boldsymbol{\xi}', \boldsymbol{\xi} \rangle \equiv \int_V \rho_0 \boldsymbol{\xi}' \cdot \boldsymbol{\xi} d^3 \mathbf{x} = \delta_{\omega', \omega}, \quad (82)$$

where $\delta_{\omega', \omega}$ is here the Kronecker delta. Together, equation (82) and equation (74) imply that the right-hand side of the linear perturbation equation (71) is self-adjoint with respect to this energy inner product. Therefore, the condition equation (81) unlimitedly stems from *both* a particular dynamical equation, and an appropriate inner product. If equation (82) is altered, which amounts to a different spatial weighting of the solutions, then equation (81) may not hold, and the time dependence of the solution may acquire spurious growth or decay.

The above four results that derive from integrating over the volume V hinge on the condition that

$$(\mathbf{u} \cdot \hat{\mathbf{n}}) P_1 = 0 \quad (83)$$

on the boundary of V with $\hat{\mathbf{n}}$ the unit normal vector. This condition is not a mere technical triviality, as equation (83) causes the divergence term in equation (74) to vanish. If V is a bounded domain, or is periodic in the horizontal direction and bounded in the vertical direction, then we may easily satisfy equation (83) by requiring $(\mathbf{u} \cdot \hat{\mathbf{n}}) = 0$ by itself (e.g., impenetrable boundaries). For the travelling waves we considered in Section 3 the product $(\mathbf{u} \cdot \hat{\mathbf{n}}) P_1$ is itself periodic and integrates to zero, since $|\mathbf{u}| \sim \rho_0^{-1/2}$, and $|P_1| \sim \rho_0^{1/2}$ for large and small atmospheric heights. As we will see in the following subsections, the far-field behavior of travelling waves controls the stability properties of different anelastic models.

4.2. ANS Energy Balance

For comparison with the total energy equation (68) for the Euler system, we now derive an equivalent energy balance for the anelastic models, beginning with the ANS

equations. Contracting equation (18) with \mathbf{u} and using the anelastic continuity equation (9) gives in basic form

$$\frac{\partial K}{\partial t} + \nabla \cdot [\mathbf{u}(K + \rho_0 \varpi)] + \rho_0 \mathbf{u} \cdot \mathbf{g} \frac{S_1}{c_p} = \varpi \rho_0 \mathbf{u} \cdot \nabla \left(\frac{S_0}{c_p} \right) \quad (84)$$

with kinetic energy density $K = \rho_0 |\mathbf{u}|^2/2$. Using the relationship A2 in Appendix A, we put the left hand side of equation (84) into conservative form

$$\frac{\partial E}{\partial t} + \nabla \cdot [\mathbf{u}(E + \rho_0 \hat{\varpi})] = \varpi \rho_0 \mathbf{u} \cdot \nabla \left(\frac{S_0}{c_p} \right), \quad (85)$$

where E and $\hat{\varpi}$ are given by equations (A4) and (A5) respectively. We cannot however transform the right-hand side into conservative form unless

$$\lim_{\tau \rightarrow \infty} \frac{1}{\tau} \int_0^\tau \int_V \varpi \rho_0 \mathbf{u} \cdot \nabla S_0 d^3 \mathbf{x} dt = 0. \quad (86)$$

This condition is not true in general and, simply stated, arbitrary (nonlinear) motions in the ANS equations do not conserve energy. Condition (86) is satisfied for adiabatically-stratified atmospheres, where $\nabla S_0 = 0$, and in those systems the ANS equations do conserve energy.

We turn now to linearized motions to learn more about the strange behavior found in Section 3.2 by considering the equivalent of equation (74) for the ANS model equations. Contracting the linear momentum equation with an arbitrary $\boldsymbol{\xi}'$, but here satisfying $\nabla \cdot (\rho_0 \boldsymbol{\xi}') = 0$ (again, $\boldsymbol{\xi}'$ could be either $\boldsymbol{\xi}$ or $\partial_t \boldsymbol{\xi} = \mathbf{u}$), produces

$$\rho_0 \left(\boldsymbol{\xi}' \cdot \frac{\partial^2 \boldsymbol{\xi}}{\partial t^2} + \frac{g^2}{N^2} \frac{S'_1 S_1}{c_p^2} \right) + \nabla \cdot (\rho_0 \boldsymbol{\xi}' \varpi) = \varpi \rho_0 \boldsymbol{\xi}' \cdot \nabla \left(\frac{S_0}{c_p} \right). \quad (87)$$

If we integrate equation (87) over the entire volume, V , then the right-hand side refuses to vanish: even linearized motions do not conserve energy in the ANS equations.

The non-vanishing right-hand side of equation (87) would also appear to imply that the squared frequencies ω^2 are not strictly real. On the surface, the asymmetric nature of equation (87) would appear to imply non-self-adjointness of the linear equations and hence spuriously growing modes. This is consistent with what we found for our analysis in an infinite isothermal atmosphere (Sec. 3.2); as we found there, a correction to the spatial structure counteracts this effect and regains real eigenvalues for the linear equations at the cost of modes which grow in spatial height. In the literature of anelastic simulations however, no mention appears of these spuriously growing gravity waves, and a paradox seems apparent (e.g., Rogers & Glatzmaier 2005b; Brun et al. 2011).

The paradox of spurious growth is remedied by the following transformation of equation (87),

$$\hat{\rho}_0 \left(\boldsymbol{\xi}' \cdot \frac{\partial^2 \boldsymbol{\xi}}{\partial t^2} + \frac{g^2}{N^2} \frac{S'_1 S_1}{c_p^2} \right) + \nabla \cdot (\hat{\rho}_0 \boldsymbol{\xi}' \varpi) = 0, \quad (88)$$

where we define the scaled pseudo-density

$$\hat{\rho}_0 = \rho_0 e^{-S_0/c_p}, \quad (89)$$

which reduces to the actual background density in the case of adiabatic stratification.

Though energy is not conserved for nonlinear dynamics, nor for linear waves, equation (88) implies that the

following pseudo-energy is conserved

$$\hat{E} = \frac{1}{2} \int_V \hat{\rho}_0 \left[|\mathbf{u}|^2 + \frac{g^2}{N^2} \left(\frac{S_1}{c_p} \right)^2 \right] d^3 \mathbf{x}, \quad (90)$$

i.e., $\partial_t \hat{E} = 0$, for *linear* perturbations. If the perturbations are *nonlinear* then the rescaling of the density fails since the advection of kinetic energy is not an exact divergence in terms of this pseudo-density.

As in the compressible case (eq. 80), one may use equations (79) & (88) to show that

$$\begin{aligned} \omega^2 \int_V \hat{\rho}_0 |\boldsymbol{\xi}|^2 d^3 \mathbf{x} &= \int_V \hat{\rho}_0 \frac{g^2}{N^2} \left| \frac{S_1}{c_p} \right|^2 d^3 \mathbf{x} = \\ & \int_V \hat{\rho}_0 \frac{N^2}{g^2} |\boldsymbol{\xi} \cdot \mathbf{g}|^2 d^3 \mathbf{x}, \end{aligned} \quad (91)$$

which implies that $\Im(\omega^2) = 0$ even if energy is not conserved. This indicates that the conservation of a pseudo-energy resolves the paradox of spurious growth and leads to purely real squared temporal frequencies ω^2 . We believe that this explains why this phenomena of pseudo-energy conservation and energy violation has been previously missed in the literature.

Equations (88) & (91) imply that the linearized ANS equations are self-adjoint under the pseudo-energy inner product, and that eigenfunctions with different frequency are orthogonal with respect to this pseudo-density weighted norm

$$\langle \boldsymbol{\xi}', \boldsymbol{\xi} \rangle_{\hat{\rho}_0} \equiv \int_V \hat{\rho}_0 \boldsymbol{\xi}' \cdot \boldsymbol{\xi} d^3 \mathbf{x} = \delta_{\omega', \omega}. \quad (92)$$

The difference between equations (82) & (92) imply that external forcings and initial conditions project onto different frequencies and basis vectors differently in the ANS equations than in the FC equations. In particular, the eigenfunctions of pseudo-energy-conserving waves in the ANS equations are different than the eigenfunctions given by energy-conserving motions (e.g., the FC equations). In strongly stably-stratified atmospheres, these differences may be dramatic, as we will encounter in Section 5

4.3. LBR Energy Balance

Unlike the ANS equations, the LBR equations show no problems with energy conservation. Contracting equation (24) with \mathbf{u} and using the anelastic continuity equation (9) gives in basic form

$$\frac{\partial K}{\partial t} + \nabla \cdot [\mathbf{u}(K + \rho_0 \varpi)] + \rho_0 \mathbf{u} \cdot \mathbf{g} \frac{S_1}{c_p} = 0. \quad (93)$$

Using the relationship A2 in Appendix A, we put equation (93) into conservative form

$$\frac{\partial E}{\partial t} + \nabla \cdot [\mathbf{u}(E + \rho_0 \hat{\varpi})] = 0, \quad (94)$$

where E and $\hat{\varpi}$ are given by equations (A4) and (A5) respectively. If we integrate this over a bounded volume V (where as in eq 83, $\mathbf{u} \cdot \hat{\mathbf{n}} = 0$) then the divergence terms vanish and arbitrary (nonlinear) motions in the LBR equations obey an energy conservation law.

For linear perturbations and for nonlinear perturbations in certain atmospheres (including adiabatic and

isothermal atmospheres), the LBR equations conserve an alternative total energy

$$\tilde{E} \equiv \frac{1}{2} \int_V \rho_0 \left(|\mathbf{u}|^2 + \frac{1}{c_p} \frac{d\Phi}{dS_0} S_1^2 \right) d^3 \mathbf{x}, \quad (95)$$

i.e. $\partial_t \tilde{E} = 0$, as detailed in Appendix A.

For linear perturbations we may furthermore write

$$\rho_0 \left(\boldsymbol{\xi}' \cdot \frac{\partial^2 \boldsymbol{\xi}}{\partial t^2} + \frac{g^2}{N^2} \frac{S_1' S_1}{c_p^2} \right) + \nabla \cdot (\rho_0 \boldsymbol{\xi}' \varpi) = 0. \quad (96)$$

This implies self-adjointness of system under the energy inner product, and also that

$$\begin{aligned} \omega^2 \int_V \rho_0 |\boldsymbol{\xi}|^2 d^3 \mathbf{x} &= \int_V \rho_0 \frac{g^2}{N^2} \left| \frac{S_1}{c_p} \right|^2 d^3 \mathbf{x} = \\ & \int_V \rho_0 \frac{N^2}{g^2} |\boldsymbol{\xi} \cdot \mathbf{g}|^2 d^3 \mathbf{x}, \end{aligned} \quad (97)$$

whence it follows that $\Im(\omega^2) = 0$. Linear motions conserve energy in the LBR equations and wavelike motions have real squared temporal frequencies ω^2 .

4.4. RG Energy Balance

For the RG equations, using similar transformations as in Sections 4.1–4.3, we obtain the following nonlinear energy balance

$$\frac{\partial E}{\partial t} + \nabla \cdot [\mathbf{u}(E + \rho_0 \hat{\varpi})] = \varpi \rho_0 \mathbf{u} \cdot \nabla \ln T_0, \quad (98)$$

where

$$E = \rho_0 \left(\frac{|\mathbf{u}|^2}{2} - \gamma \Phi \frac{T_1}{T_0} \right), \quad (99)$$

$$\hat{\varpi} = \varpi - \frac{\gamma}{c_p} \int_a^r \Phi(r) dS_0(r). \quad (100)$$

It is not possible to cast the right-hand side of equation (98) into conservative form except in the specialized case of isothermal atmospheres where $\nabla \ln T_0 = 0$. This contrasts with the ANS equations, which can only be written in conservative form in adiabatic atmospheres. Thus the RG equations do not conserve energy for either anelastic convection or gravity wave dynamics in arbitrary atmospheres.

Linear perturbations to these equations do nevertheless obey a pseudo-density weighted self-adjointness

$$\hat{\rho}_0 \left(\boldsymbol{\xi}' \cdot \frac{\partial^2 \boldsymbol{\xi}}{\partial t^2} + \frac{g^2}{\gamma N^2} \frac{T_1' T_1}{T_0^2} \right) + \nabla \cdot (\hat{\rho}_0 \boldsymbol{\xi}' \varpi) = 0, \quad (101)$$

where

$$\frac{T_1}{T_0} = -\gamma \boldsymbol{\xi} \cdot \nabla \left(\frac{S_0}{c_p} \right), \quad (102)$$

and the pseudo-density becomes

$$\hat{\rho}_0 = \frac{\rho_0}{T_0}. \quad (103)$$

Furthermore, as in Sections 4.1–4.3, we find that

$$\omega^2 \int_V \hat{\rho}_0 |\boldsymbol{\xi}|^2 d^3\mathbf{x} = \int_V \hat{\rho}_0 \frac{g^2}{\gamma N^2} \left| \frac{T_1}{T_0} \right|^2 d^3\mathbf{x} = \gamma \int_V \hat{\rho}_0 \frac{N^2}{g^2} |\boldsymbol{\xi} \cdot \mathbf{g}|^2 d^3\mathbf{x}. \quad (104)$$

Equation (104) implies that $\Im(\omega^2) = 0$ even if energy is not conserved. As in the ANS equations, waves in the RG equations have real squared temporal frequencies ω^2 in volumes where $\hat{\rho}_0(\boldsymbol{\xi} \cdot \hat{\mathbf{n}})\varpi = 0$ on the domain boundaries, but the eigenfunctions and energies are weighted by pseudo-density (103).

Equation (104) implies that the stability *boundary* for the fully compressible and other anelastic models, $N^2 = 0$, remains unaltered in the RG equations in spite of energy non-conservation. Two problems do however still remain. The first is that an extra factor of γ appears in the last integral of equation (104). As we found for waves in an isothermal atmosphere, this leads to frequencies that are too high. The second more serious issue is that energy is not conserved *unless* the background atmosphere is isothermal. In particular, both linear and nonlinear motions within adiabatically-stratified atmospheres will not conserve energy.

5. BOUNDED ATMOSPHERES AND IMPLEMENTATION IN SPHERICAL SYSTEMS

We now turn to considering gravity waves in a spherical shell. In this geometry divergence at infinity is no longer a problem. We will find that impenetrable boundary conditions at the top and bottom of the spherical shell lead to frequencies that are purely real (e.g., oscillating waves only, with no spuriously growing modes) but now the eigenfunctions will be severely distorted in the ANS equations as compared with the LBR equations. In a sense, the eigenfunctions try to diverge to infinity but are constrained by the boundary conditions. Analytic eigenfunctions can be found if we consider a simplified atmosphere with constant gravity $\mathbf{g} = -g\hat{\mathbf{r}}$ and constant Brunt-Väisälä frequency N . In an isothermal atmosphere with temperature T_0 this can be achieved by setting the entropy gradient to

$$\nabla_r S_0 = \frac{\partial S_0}{\partial r} = \frac{g}{T_0}. \quad (105)$$

The background entropy S_0 is found by integration, with the arbitrary constant set by a reference value within the atmosphere (here at the base of the domain). The background pressure and density are determined by hydrostatic balance and their values at the reference layer. We first derive the analytic solutions and then compare these solutions with fully nonlinear calculations using two versions of the anelastic spherical harmonic (ASH) code.

5.1. Modes in stratified isothermal spherical shells

We begin by obtaining analytic solutions for the low-Mach number ANS, LBR, and RG equations. Full details are given in Appendix B. Motivated by the properties of the solar radiative zone, we solve for the eigenvalues of the low-Mach number anelastic equations within a spherical shell stretching from $a = 0.50R_\odot$ to $b = 0.70R_\odot$ with r_\odot the solar radius. This shell has geometric extent

$$\chi = \frac{a}{b} = 0.717 \quad (106)$$

Table 4
Atmosphere parameters

n_ρ	$\Delta S/c_P$	H <i>Mm</i>	H R_\odot	T_0 $10^6 K$	N $10^{-3} s^{-1}$	τ_{BV} s
0.25	0.1	548	0.788	39.3408	0.84	1185
1.0	0.4	137	0.197	9.83520	1.69	592.6
2.5	1	54.8	0.0788	3.93408	2.66	374.6
5.0	2	27.4	0.0394	1.96704	3.77	264.9
7.5	3	18.3	0.0263	1.31136	4.62	216.3
10.0	4	13.7	0.0197	0.98352	5.34	187.4
12.5	5	11.0	0.0158	0.78682	5.96	168.5

Note. — Quoted are the number of density scale heights in the domain n_ρ , the non-dimensional entropy drop across the shell $\Delta S/c_P$, the physical size of the density scale height H in megameters and relative to the solar radius, the isothermal temperature T_0 , the constant Brunt-Väisälä frequency N and the corresponding timescale $\tau_{BV} = 1/N$. In all models, $r_{\text{bot}} = a = 210Mm \approx 0.30R_\odot$ and $r_{\text{top}} = b = 485Mm \approx 0.70R_\odot$, with $\chi = a/b = 0.433$ and with the solar radius $r_\odot = 695Mm$. Additional simulations conducted at $\Delta S/c_P = 10^{-2}$, 10^{-3} and 10^{-4} are not shown here.

Table 5
Isothermal atmosphere solutions

	k_1	k_2	k_3	k_4	k_5
$n_\rho = 2.5$					
ANS	9.72953	19.0635	28.4829	37.9246	47.3752
LBR	10.1839	19.3017	28.6431	38.045	47.4717
$n_\rho = 5$					
ANS	10.4846	19.4637	28.7527	38.1277	47.5379
LBR	12.0834	20.3817	29.3825	38.605	47.9216
$n_\rho = 7.5$					
LBR	14.6998	22.0671	30.5764	39.5211	48.6627
ANS	11.6324	20.1134	29.1969	38.4639	47.8080
FC-1	2.16693	15.4867	26.2203	36.2565	46.0510
FC-∞	9.49926	18.6646	27.9660	37.3421	46.7676
$n_\rho = 12.5$					
ANS	14.692	22.0618	30.5726	39.5182	48.6602
LBR	20.888	26.7604	34.1169	42.3167	50.9577

Note. — Radial wavenumbers for gravity waves in selected bounded isothermal atmospheres listed in Table 4. Quoted are the five lowest wavenumbers k_1 – k_5 in each equation set. In the full Euler equations, the radial wavenumber depends on spherical harmonic ℓ ; as such, we quote wavenumbers at low and high values of ℓ (FC-1 at $\ell = 1$ and FC-∞ at $\ell = 50$ respectively). The RG equations have the same eigenfunctions and radial wavenumbers as the LBR equations and are not separately quoted.

and we consider several different values for the scale height H and number of density scale heights n_ρ . The atmospheric parameters are reported in Table 4. The first five such wavenumbers for the ANS and LBR equations are presented in Table 5 for several of these atmospheres.

We begin by discussing eigenfunctions in the $n_\rho = 7.5$ atmosphere, as this atmosphere will form the primary comparison case for the 3-D numerical simulations in Section 5.2. In Figure 2 we show both the fundamental k_1 mode and a higher-order k_5 mode. In addition to the various low-Mach number anelastic eigenfunctions, here we also overplot eigenfunctions for the fully compressible Euler (FC) equations; and these require numeric solu-

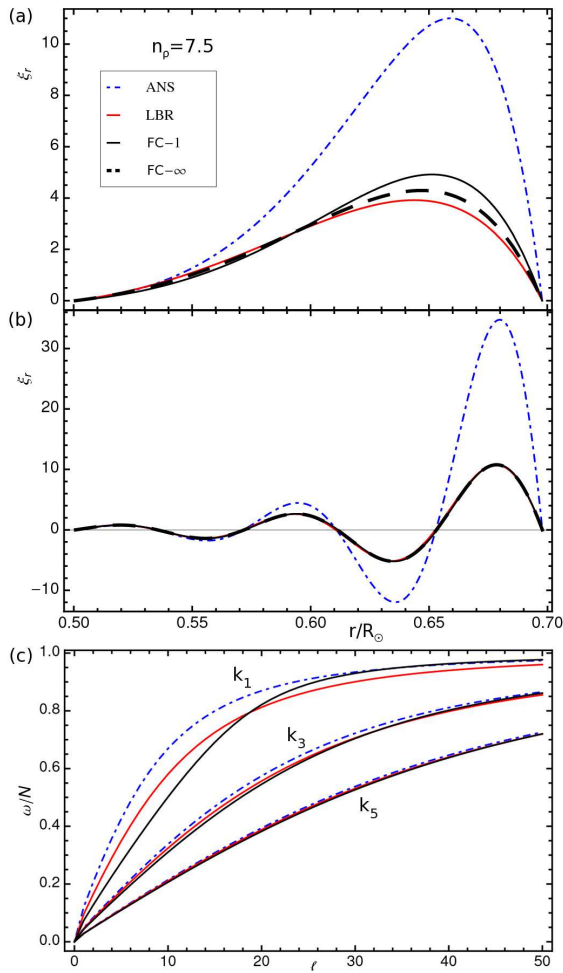


Figure 2. Eigenfunctions for the $n_\rho = 7.5$ atmosphere. (a) Eigenfunctions for the fundamental k_1 mode and (b) the higher-order k_5 mode. (c) Dispersion relationship ω/N for the first, third and fifth radial modes (k_1, k_3, k_5), with lower- k having higher ω . In each plot, the ANS equations are shown in blue (dash-dotted) while the LBR equations are shown in red (solid). The full compressible results are shown in black. For the eigenfunctions, the solid line corresponds to $\ell = 1$ (FC-1) and the thick dashed line corresponding to $\ell = 50$ (FC-∞).

tions. In the full FC equations, the radial eigenfunction depends on spherical harmonic ℓ , whereas in the anelastic equation sets this coupling disappears. This effect is most pronounced in the FC eigenfunctions at low- ℓ , with the eigenfunctions largely becoming constant with ℓ when $\ell \gg k$. As such, we plot two FC eigenfunctions, one at $\ell = 1$ (FC-1) and one at $\ell = 50$ (FC-∞).

As is clearly evident in Figure 2b, the discrepancies in the ANS eigenfunctions do not diminish at high radial wavenumbers. This continues to hold true for higher wavenumbers than we show here. This is not surprising, as these discrepancies arise from the energy non-conservation in the ANS equations, rather than from assumptions about the relative size of the gravity wavelengths and scale heights in the atmosphere. In contrast, at high- k , the other equation sets all converge. The dispersion relationship for odd modes k_1, k_3 and k_5 are shown as a function of spherical harmonic ℓ in Figure 2(c). For the k_1 mode and at low- ℓ , the low-Mach

number anelastic equations generally produce higher frequencies than the full compressible Euler equations. At higher- ℓ all of these frequencies converge to the Brunt-Väisälä frequency N , and the frequencies in the ANS and LBR equations generally cross the frequencies of the Euler equations at some moderate ℓ . The frequencies converge much sooner at high radial order (e.g., k_5). The RG equations are not shown in Figure 2; their frequencies are consistently a factor of $\sqrt{\gamma} \approx 1.3$ larger than the LBR equations.

The eigenfunctions of the fundamental mode k_1 are shown in Figure 3 for several isothermal atmospheres from Table 4. With the normalization that we have chosen (Appendix B), the ANS eigenfunctions are generically larger in amplitude than the other systems of equations. This difference is most pronounced near the top of the domain, and the discrepancies grow as the amount of stratification grows.

5.2. Numerical models with the ASH code

We turn now to fully nonlinear 3-D simulations of gravity wave propagation using the ASH code. We study gravity waves in ASH using both the standard ANS equations as well as an implementation of the LBR equations. In the ASH-ANS equations, the momentum and energy equations are

$$\rho_0 \left[\frac{\partial \mathbf{u}}{\partial t} + \mathbf{u} \cdot \nabla \mathbf{u} \right] = -\nabla P_1 + \rho_0 \frac{P_1}{\gamma P_0} \mathbf{g} - \rho_0 \frac{S_1}{c_p} \mathbf{g} - \nabla \cdot \mathcal{D}, \quad (107)$$

$$\frac{\partial S_1}{\partial t} + \mathbf{u} \cdot \nabla S_1 = -\mathbf{u} \cdot \nabla S_0 + \frac{1}{\rho_0 T_0} \nabla \cdot [\kappa \rho_0 T_0 \nabla S_1] + 2 \frac{\nu}{T_0} \left[e_{ij} e_{ij} - \frac{1}{3} (\nabla \cdot \mathbf{u})^2 \right], \quad (108)$$

where the viscous stress tensor is

$$\mathcal{D}_{ij} = -2\rho_0 \nu \left[e_{ij} - \frac{1}{3} (\nabla \cdot \mathbf{u}) \delta_{ij} \right], \quad (109)$$

with e_{ij} the strain rate tensor and δ_{ij} the Kronecker delta. These anelastic equations assume a linearized equation of state (eq 11) and the anelastic constraint (eq 9) but are otherwise fully nonlinear. The ASH-LBR equations are identical except for the momentum equation, where

$$\rho_0 \left[\frac{\partial \mathbf{u}}{\partial t} + \mathbf{u} \cdot \nabla \mathbf{u} \right] = -\rho_0 \nabla \left(\frac{P_1}{\rho_0} \right) - \rho_0 \frac{S_1}{c_p} \mathbf{g} - \nabla \cdot \mathcal{D}. \quad (110)$$

All other properties of the simulations are identical.

We take the geometry and atmosphere used previously in this section for the background reference state entropy S_0 , pressure P_0 , temperature T_0 , and density ρ_0 . These quantities vary in radius but do not evolve in time. Here we first focus on simulations conducted in an isothermal atmosphere with $n_\rho = 7.5$ and with other parameters given in Table 4. In comparison, over the same range of radii in the Sun $n_{\rho, \odot} \approx 1.8$, while $n_{\rho, \odot} \approx 6.6$ over the whole solar radiative zone. As such, the results presented here are likely an over-estimate for comparable effects in the solar interior, but the larger number of scale heights more clearly emphasizes the differences between the ASH-ANS and ASH-LBR equations. We will return to solar conditions at the end of this section.

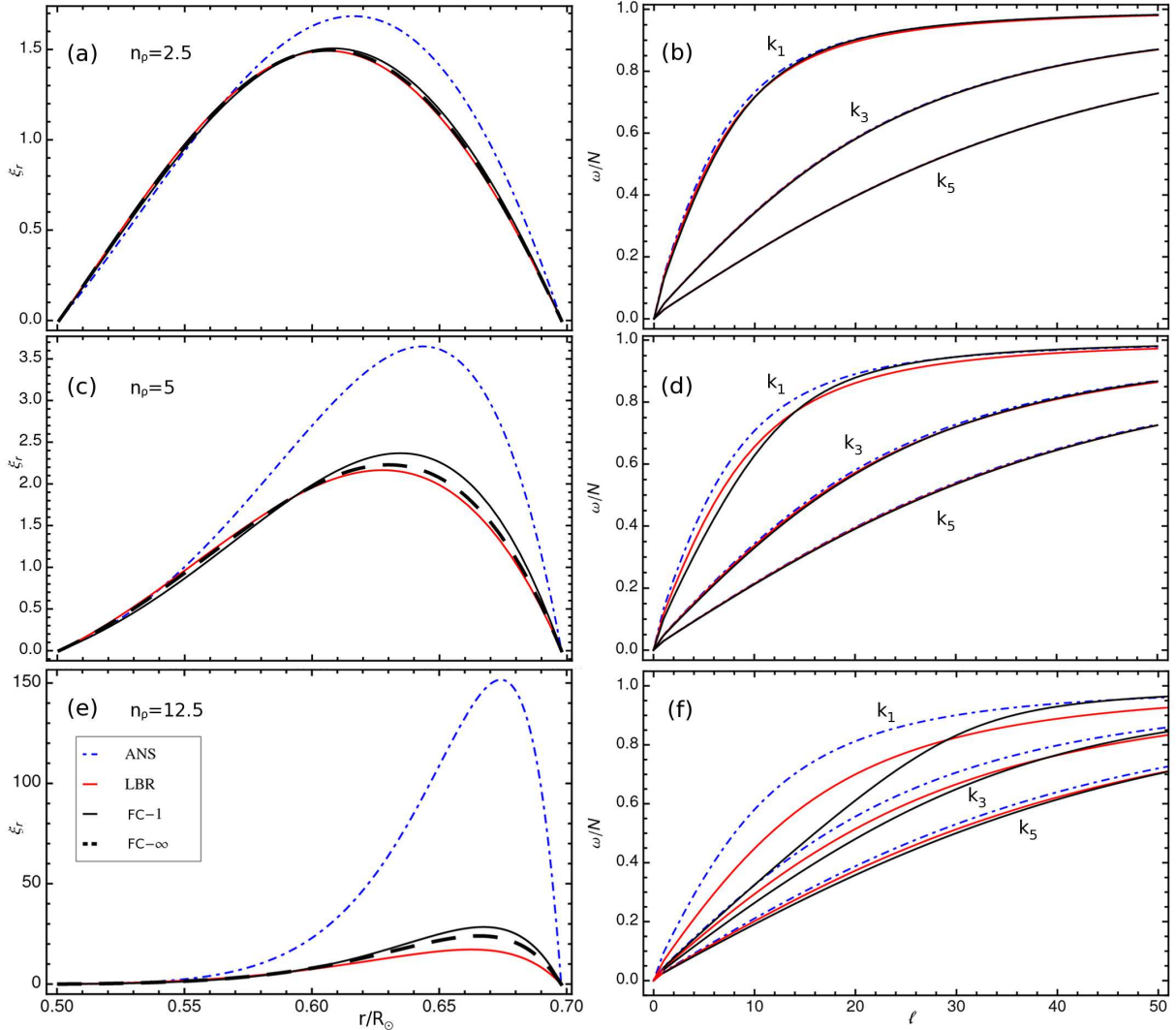


Figure 3. Eigenfunctions and dispersion relationships for selected isothermal atmospheres. In (a, b) $n_\rho = 2.5$, in (c, d) $n_\rho = 5$, and in (e, f) $n_\rho = 12.5$. Eigenfunctions for the fundamental k_1 mode are shown in (a, c, e) and dispersion relationships for the k_1 , k_3 and k_5 radial modes are shown in (b, d, f). Labels for lines in all plots are given in (e).

In the pseudo-energy conserving ANS equations, the scaled pseudo-density (eq 89) is weighted by the background entropy S_0 . As such, the non-dimensional entropy drop across the domain

$$\Delta S/c_P = \frac{1}{c_P} (S_0(r_{\text{top}}) - S_0(r_{\text{bot}})), \quad (111)$$

or the number of pseudo-density scale heights $n_{\hat{\rho}}$ with

$$n_{\hat{\rho}} = n_\rho + \Delta S/c_P, \quad (112)$$

are both likely better measurements of how much pseudo-energies differ from energies in the ANS equations than the number of density scale heights n_ρ in the atmosphere. For a non-isothermal atmosphere, we can use the equation of state (6) to obtain

$$n_{\hat{\rho}} = \frac{2\gamma - 1}{\gamma} n_\rho - \frac{1}{\gamma} n_T, \quad (113)$$

where $n_T = \ln(T_{0,\text{bot}}/T_{0,\text{top}})$ is the number of temperature scale heights. In an isothermal atmosphere with $\gamma = 5/3$, this reduces to $n_{\hat{\rho}} = (7/5)n_\rho$ and the number of ANS pseudo-density scale heights always exceeds the

number of density scale heights. Our isothermal atmosphere with $n_\rho = 7.5$ has $\Delta S/c_P = 3$ and $n_{\hat{\rho}} = 10.5$.

The numerical simulations were conducted in a non-rotating system with viscosity $\nu = 1 \times 10^{10} \text{cm}^2/\text{s}$ and entropy diffusivity $\kappa = 4 \times 10^{10} \text{cm}^2/\text{s}$ and with $c_P = 3.4 \times 10^8 \text{ergs g}^{-1} \text{K}^{-1}$. In contrast to ASH simulations of stellar convection (e.g., Brown et al. 2008; Miesch et al. 2008), in these isothermal atmosphere simulations we neglect radiative diffusion of temperature in the entropy equation and diffusion of the background entropy gradient ∇S_0 , which in these simulations is set by equation (105). As such, there is no energy flux through the simulation. The velocity boundary conditions at the top and bottom of the domain are stress-free and impenetrable, and the thermal boundaries maintain a constant entropy gradient. All simulations are conducted with a resolution of $257 \times 256 \times 512$ ($N_r \times N_\theta \times N_\phi$), with all functions expanded in Chebyshev polynomials radially and spherical harmonics horizontally; this leads to a dealiased spectral resolution of $\ell_{\text{max}} = 170$, which resolves the wave motions studied here.

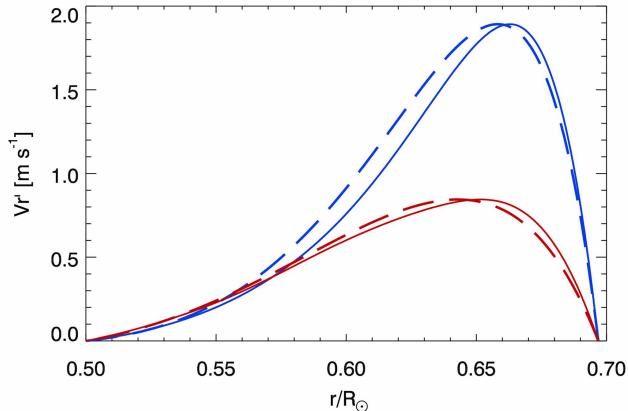


Figure 4. Fluctuating velocities in numerical simulations for the $n_\rho = 7.5$ isothermal atmosphere. Shown are the rms radial velocities for ASH simulations calculated with ANS (blue, solid) and LBR (red, solid) treatments of the momentum equation. The thick dashed lines give the analytic k_1 eigenmode for each equation set, normalized by the peak velocity realized in the ASH simulations.

Timestepping errors can have important impacts on the properties of wave motions. The ASH code uses a second-order Adams-Bashforth/Crank-Nicolson technique for time evolution, which treats diffusive processes implicitly and advective processes explicitly. In our studies here, we found that it is crucial that the advective interactions between the wave motions and the background reference state stratification be handled implicitly (on the Crank-Nicolson side). In the entropy equation (108), this term is

$$\mathbf{u} \cdot \nabla S_0.$$

If these interactions are handled explicitly (via the Adams-Bashforth portion) then the solutions are sensitive to the size of the timestep; with sufficiently small timesteps a solution can be time-evolved correctly, but these timesteps must be nearly an order of magnitude smaller than are otherwise possible. Larger timesteps lead to explicit timestep errors that grow quickly in the solution. Handling these interactions implicitly, as we do here, leads to much more stable behavior. To simplify matters, in these studies we fix the timestep at slightly less than one third of the Brunt-Väisälä timescale τ_{BV} (e.g., 70s in the $n_\rho = 7.5$ atmosphere).

At the start of each simulation, random entropy perturbations are introduced in a band of spherical harmonic ℓ ranging from $\ell = 1$ –30, at all spherical harmonic m values. The radial perturbation has two bumps in radius, defined by

$$f(r) = 1 - 3x^2 + 3x^4 - x^6 + 2.5x - 2.5x^3, \quad (114)$$

with scaled radius x given by

$$x = (2r - r_{\text{top}} - r_{\text{bot}})/(r_{\text{top}} - r_{\text{bot}}), \quad x \in [-1, 1]. \quad (115)$$

This radial perturbation does not exactly match the radial eigenfunction of the gravity waves but rather drives a broad band of such waves with the largest power in the lowest k_1 and k_2 modes. The initial perturbations lead to flows of roughly 1 m s^{-1} in amplitude, with Reynolds numbers $Re = uL/\nu$ of about 100. The viscous Q of

these waves,

$$Q \equiv \frac{\omega L^2}{\nu} \approx 8.67 \times 10^7 \quad (116)$$

where we have taken $\omega \approx N$ (the low-frequency $\ell = 1$ fundamental mode has $\omega \approx 0.12N$) and $L = r_{\text{top}} - r_{\text{bot}}$, the depth of our shell. A thermal Q would be four times smaller. The Q calculated in equation (116) is most applicable to our longest wavelength modes; our shortest wavelength modes with $\ell = 30$ would have a Q of about

$$Q_{30} = \frac{Q}{\ell(\ell+1)} \approx 9.32 \times 10^4, \quad (117)$$

which is still quite large. Thus, we expect that the gravity waves should only be very weakly damped by diffusion.

5.3. Eigenfunctions and violation of energy conservation

We expect that there will be two clear effects from the choice of ANS or LBR equations. The first such effect is that radial eigenfunctions of the two systems should differ strongly, as discussed in Section 5.1. The radial eigenfunctions for the ASH-ANS and ASH-LBR simulations are shown in Figure 4. Plotted on the same scale and against radius are fluctuating rms radial velocities Vr' at a time late in the simulations (30 days after initiation, or roughly 12,000 τ_{BV}). These rms velocities are further time-averaged over roughly 2.5 days or about 1000 τ_{BV} .

Overplotted on each simulation is the appropriate radial eigenfunction corresponding to the gravest k_1 mode for the ANS or LBR equations. Here the eigenfunctions are scaled by the peak rms velocity. In both simulations, the rms velocities from the fully nonlinear 3-D numerical simulations agree very well with the analytic eigenfunctions. In the ASH-ANS set of equations, the radial velocities peak more strongly in the upper portion of the domain, reaching amplitudes 2-4 times larger than the ANS-LBR equations. The fluctuating velocities differ strongly, as expected.

The second effect is that, as discussed in Section 4, the LBR equations should conserve energy while the ANS equations conserve a pseudo-energy. In the simulations we define volume-averaged total energy E , kinetic energy K and potential energy U densities

$$E = K + U, \quad (118)$$

$$K = \frac{1}{V} \int \frac{1}{2} \rho_0 u^2 dV, \quad (119)$$

$$U = \frac{1}{V} \int \frac{1}{2} \rho_0 g \left(\frac{\partial S_0}{\partial r} \frac{S_0}{c_P} \right)^{-1} \left(\frac{S_1}{c_P} \right)^2 dV, \quad (120)$$

with fluctuating velocity u and fluctuating entropy S_1 , and where the integral is over the full simulation volume V (e.g., eqn 95). Likewise we define pseudo-energy densities (e.g., eqn 90)

$$PE = PK + PU, \quad (121)$$

$$PK = \frac{1}{V} \int \frac{1}{2} e^{-S_0/c_P} \rho_0 u^2 dV, \quad (122)$$

$$PU = \frac{1}{V} \int \frac{1}{2} e^{-S_0/c_P} \rho_0 g \left(\frac{\partial S_0}{\partial r} \frac{S_0}{c_P} \right)^{-1} \left(\frac{S_1}{c_P} \right)^2 dV. \quad (123)$$

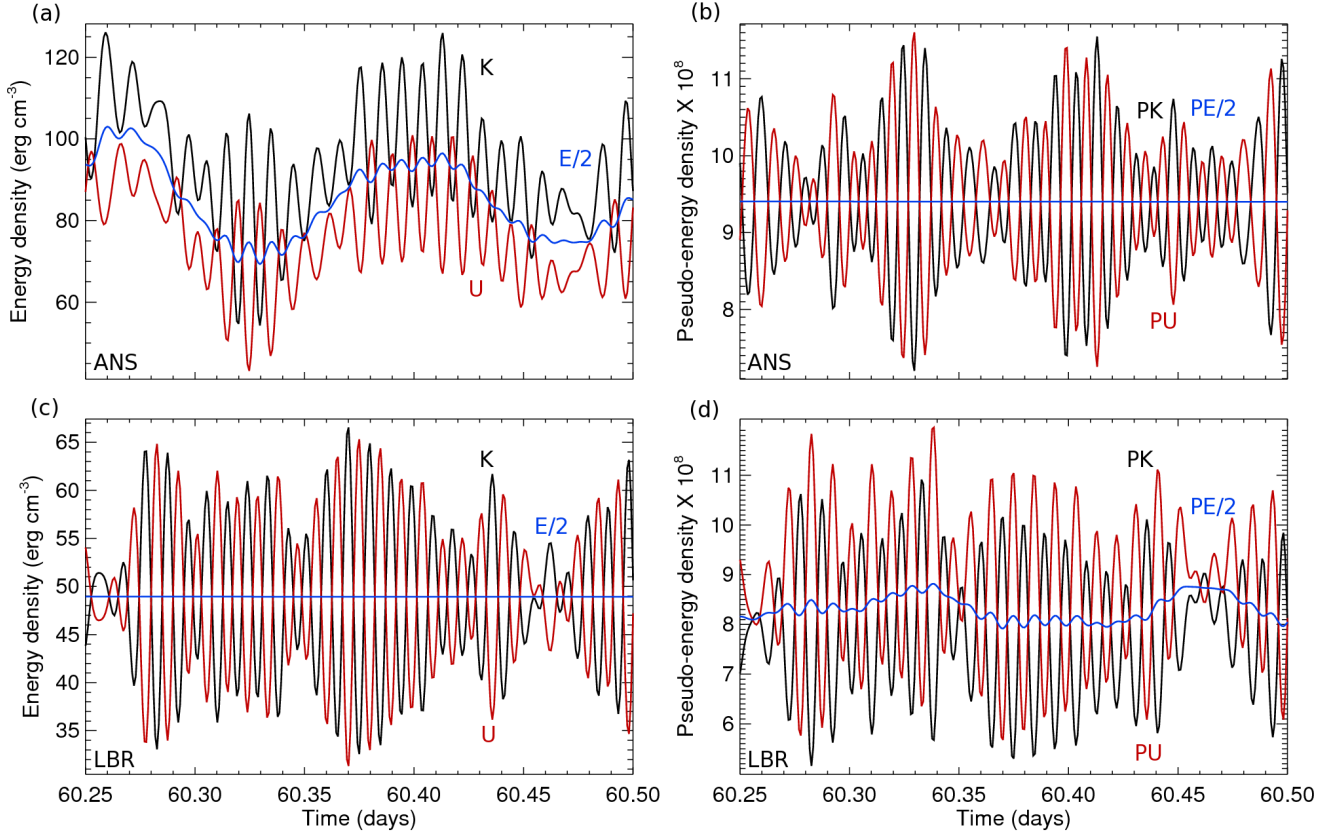


Figure 5. Temporal evolution of energies and pseudo-energies, shown over identical intervals for ASH-ANS and ASH-LBR. (a) Energy and (b) pseudo-energy in ASH-ANS simulation, with definitions as given in equations (118–123). Pseudo-energy densities are here multiplied by 10^8 . The total energy E and pseudo energy PE is divided by 2 to highlight the fluctuations between K and U or PK and PU respectively. The ASH-ANS equations clearly do not conserve energy E but clearly do conserve pseudo-energy PE . Over the interval shown, $\Delta E \approx 0.101$ while $\Delta PE < 10^{-5}$, as defined in equation (124). (c) Energy and (d) pseudo-energy for ASH-LBR simulation. Energy is clearly conserved in this system, while pseudo-energy is not, with $\Delta E < 10^{-6}$ while $\Delta PE \approx 0.03$. The temporal interval shown in all plots spans about $100\tau_{BV}$ and begins about $24,000\tau_{BV}$ after the start of the simulations.

In an isothermal atmosphere with constant Brunt-Väisälä frequency N , S_0 is a function of radius and the stratification term cannot be factored out of the integral. If thermal and viscous diffusion can be neglected, E should be conserved in the LBR equations while PE will vary in time. Likewise, the ANS equations should conserve total pseudo-energy PE but should fail to conserve total energy E . Indeed, this is what we find.

Shown in Figure 5 are temporal traces of energy and pseudo-energy in the ASH-ANS simulation and the simulation using the ASH-LBR equations. Here a short interval, spanning about $100\tau_{BV}$, is shown from a much longer simulation. The wave periods are generally longer than τ_{BV} , owing to their long horizontal wavelengths. The ASH-ANS simulation shows large variations in kinetic and potential energies K and U and does not conserve total energy E (Fig. 5(a)). This simulation does however clearly conserve total pseudo-energy PE (Fig. 5(b)). Over much longer intervals of time, both the total energy and total pseudo-energy decay dissipatively. In contrast, the ASH-LBR simulation correctly conserves energy E (Fig. 5(c)) while the pseudo-energy PE fluctuates in time (Fig. 5(d)).

We define the relative energy variation ΔE and

pseudo-energy variation ΔPE as

$$\Delta E = (\delta E)/\langle E \rangle, \text{ and } \Delta PE = (\delta PE)/\langle PE \rangle, \quad (124)$$

with δ signifying the standard deviation in time and brackets denoting a time average over the same period. Subtracting off the slow diffusive decay, we find that over a ten-day interval ($4000\tau_{BV}$), $\Delta E \approx 5.6\%$ in the ASH-ANS simulation (during the interval shown in Figure 5, $\Delta E \approx 10.1\%$). Over the same interval, $\Delta PE < 0.001\%$. In contrast, the ASH-LBR simulation has $\Delta E < 0.0001\%$ and $\Delta PE \approx 3\%$ over the same ten-day interval of time. We have conducted similar simulations with diffusivities ν and κ ten times larger (e.g., $Re \approx 10$) and find a similar level of variability, and thus conclude that our results are not strongly dependent on the level of diffusivity employed. For the linear waves considered here, we find that ΔE and ΔPE are independent of the initial perturbation amplitude.

In these many-wave simulations, the introduced waves span varying portions of the frequency dispersion relationship, including regions where ω depends almost linearly on ℓ and regions where it does not (e.g., Figure 2(c)). Thus we might expect a collection of these very linear waves to behave as incoherent oscillators and that the relative energy variations for many waves might

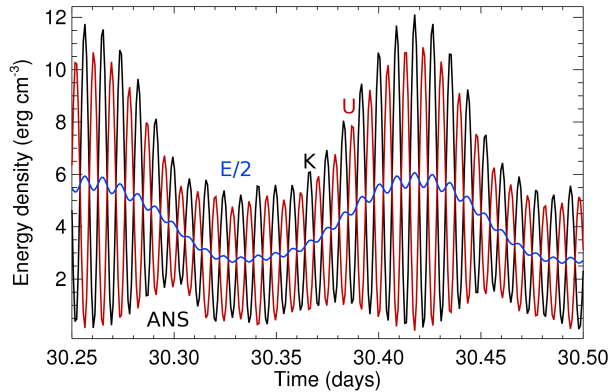


Figure 6. Relative energy variation ΔE in the single-wave ASH-ANS solution for the atmosphere with $n_\rho = 7.5$ and $\Delta S/c_P = 3$. This should be compared with Figure 5(a). Generally, the variations in these single wave solutions are about a factor of 5 larger than the many-wave solutions.

be smaller than those of any individual horizontal wave.

This is confirmed by simulations where only a single spherical harmonic perturbation is initially introduced, as shown by traces of E , K and U in Figure 6 for the $n_\rho = 7.5$ and $\Delta S/c_P = 3$ atmosphere. In this ASH-ANS simulation, only $\ell = 30$ waves (at all $|m| < \ell$) are initially excited, with the same radial perturbation as the many-wave simulations (eq 114). Hereon, we will refer to these as single-wave solutions. Comparing Figure 6 with the corresponding many-wave solution in Figure 5(a) it is clear that the relative energy variation is significantly greater. Here, $\Delta E \approx 25\%$ (ΔPE remains negligible). We have studied single-wave solutions with different horizontal wavelengths, sampling in the range from $\ell = 1$ to $\ell = 100$ and find that this level of energy variation is reasonably representative for individual waves of any horizontal wavelength in this range. This confirms our understanding that the phenomenon of energy non-conservation is due to the level of stratification and does not depend strongly on the particulars of any single mode (e.g., horizontal or vertical wavelength).

We now turn to considering isothermal atmospheres with differing levels of stratification, ranging from $n_\rho = 0.1$ –12.5 and $\Delta S/c_P = 0.1$ –5 (see Table 4). The configurations of the simulations are the same as previously discussed, though at large stratification ($n_\rho \geq 10$) a higher resolution was used, with $N_r = 1025$ and a dealiased horizontal resolution of $\ell_{\max} = 340$.

The time-averaged relative energy variations in these ASH-ANS simulations are shown in Figure 7, which displays both many-wave solutions ($\ell = 1$ –30, triangles) and single-wave solutions ($\ell = 30$, squares). The many-wave solutions span from $\Delta S/c_P = 0.4$ –5, while the single-wave solutions span a wider range from $\Delta S/c_P = 0.0001$ –5. As the stratification increases, energy non-conservation becomes increasingly significant in the ASH-ANS equations, with ΔE approaching 10% in the many-wave simulation with $n_\rho = 12.5$ and $\Delta S/c_P = 5$ and $\Delta E \approx 43\%$ in the corresponding single-wave solution. Generally, we find that the relative energy variations are about 5 times higher in the single-wave solutions than the corresponding many-wave solutions, indepen-

dent of stratification. In the corresponding ASH-LBR simulations (not shown), energy is always well conserved with $\Delta E < 10^{-6}$.

Unsurprisingly, the relative energy variation is smaller in less stratified atmospheres. At very low levels of stratification ($\Delta S/c_P \rightarrow 0$) the ratio of pseudo-density and density is almost constant throughout the domain (eq 89), and we should expect the pseudo-energy conserving ASH-ANS equations to also conserve energy fairly well. Indeed, this is what we find. As shown for single-wave solutions in Figure 7(a), at low values of $\Delta S/c_P$, the energy variation ΔE is also small ($\Delta E \approx 5 \times 10^{-5}$ at $\Delta S/c_P = 0.001$). With increasing stratification, ΔE in the single-wave ASH-ANS solutions scales almost linearly with $\Delta S/c_P$ up through $\Delta S/c_P = 0.1$. At $\Delta S/c_P = 0.4$ $\Delta E \approx 1\%$ in the single-wave solution and $\Delta E \approx 0.2\%$ in the many-wave solution. There is a change in the scaling for both single-wave and many-wave solutions at $\Delta S/c_P \approx 1$, apparent in both Figures 7(a,b); we do not understand the origin of this behavior. In all cases shown here, $\Delta PE \ll \Delta E$, and generally $\Delta PE \sim 10^{-5}$ – 10^{-6} . This floor on ΔPE likely reflects aspects of our data analysis technique and we feel that our current approach is insufficient to reliably measure energy variations in cases where $\Delta S/c_P \lesssim 10^{-4}$.

5.4. Nonlinear interactions

At much lower levels of diffusivity, or at larger initial amplitudes, the gravity waves may begin to interact nonlinearly. This is also likely to occur when the gravity waves are driven by overshooting convection from below (e.g., Mihalas & Toomre 1981). To confirm the linear nature of the waves we have studied here, we define a Froude number Fr as

$$Fr = \frac{|\nabla \times \mathbf{u}|}{N}, \quad (125)$$

or the ratio of local vorticity to the Brunt-Väisälä frequency N . This corresponds to the vorticity criteria for nonlinearity in Mihalas & Toomre (1981). We find here that Fr attains a peak value of about 5×10^{-5} in the $n_\rho = 7.5$ ASH-ANS simulation and of about 1×10^{-5} in the corresponding ASH-LBR simulation. Thus the waves studied here are quite linear. For linear waves, the Froude number gives the characteristic amplitude of all fluctuations. Owing to this, despite the large stratifications studied here ($\Delta S/c_P \sim 1$), the thermodynamic fluctuations remain quite small ($S_1/c_P \sim 10^{-5}$).

When nonlinear interactions become important, we might expect that the non-conservation of energy may cause ASH-ANS simulations to diverge even further from simulations which do conserve energy (e.g., the ASH-LBR equations). As discussed in Section 4.2, the conservation of pseudo-energy also vanishes when nonlinearity is important. Energy is conserved in the nonlinear LBR equations, but neither the pseudo-energy nor the energy is conserved in the nonlinear ANS equations. If the pseudo-energy is also not conserved, it may be possible to *inject* pseudo-energy into otherwise closed systems; alternatively, the energy and pseudo-energy may leak away without coupling to the reservoir of internal energy. Either case leads to physical inconsistencies.

Lastly, the transport by nonlinear processes in the ANS equations is likely to be very different from that

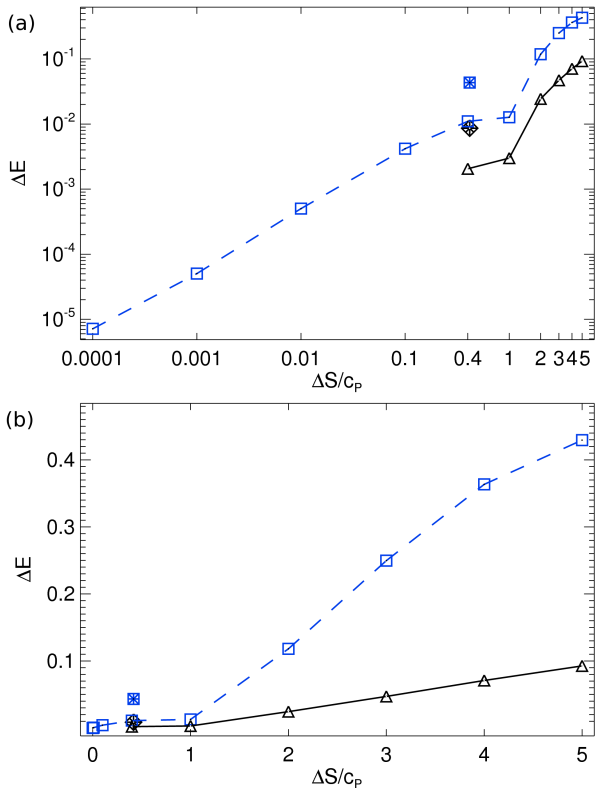


Figure 7. Violation of energy conservation in ASH-ANS simulations in various atmospheres. (a) Relative energy variation ΔE as given in equation (124) for isothermal atmospheres with different non-dimensional energy drops $\Delta S/c_p$ in log-log plot. (b) Same, in linear plot, emphasizing the behavior at large $\Delta S/c_p$. Shown in both are solutions with a single horizontal wave ($\ell = 30$, blue squares) and solutions with many horizontal waves ($\ell = 1-30$, black triangles). Also shown are solutions in a solar radiative zone atmosphere stretching from $0.5-0.7R_\odot$, with a single-wave solution (blue square with asterisk) and a many-wave solution (black diamond with asterisk). All solutions are time-averaged over an interval of $2000\tau_{BV}$, generally beginning about $200\tau_{BV}$ after the start of the simulation.

in equations that do conserve energy, as the eigenfunctions of gravity waves in the ANS equations are significantly higher in amplitude in the upper domain of stably-stratified atmospheres (Figures 2–4). This will also have important implications for mode coupling, for the steepening and breaking of gravity waves, and for all other problems where the shape of the eigenfunction itself is important.

5.5. Solar atmospheres

The results presented here so far have been for the special case of an isothermal atmosphere. The solar radiative zone is stably stratified, but has fewer density scale heights than have been considered in most of this section. Across the entire solar radiative zone

$$(\Delta S/c_p)_\odot = \int_{0.0R_\odot}^{0.7R_\odot} \frac{1}{c_p} \frac{\partial S_0}{\partial r} \approx 1.3, \quad (126)$$

and $n_{\hat{\rho},\odot} \approx 7.9$, while $\Delta S/c_p \approx 0.42$ and $n_{\hat{\rho},\odot} \approx 2.3$ over the shell geometry that we consider here ($0.5-0.7R_\odot$).

To constrain our results, we have repeated these gravity wave rundown ASH-ANS and ASH-LBR simulations

in the solar radiative interior. We take our model atmosphere from the CESAM code (Brun et al. 2002). We keep the same values of ν and κ and continue to neglect radiative diffusion acting on the fluctuating flows. A large scale radiative diffusion based on the Rossland mean-opacity is included that acts on ∇T_0 and there is a flux equal to the solar flux throughout the domain. We keep the same choice of r_{top} and r_{bot} , thus $n_\rho \approx 1.8$ and $\Delta S/c_p \approx 0.417$.

These solar simulations are shown in Figure 7(a) as asterisks. In this model solar atmosphere, we find that in many-wave solutions ($\ell = 1-30$) with the ASH-ANS equations $\Delta E \approx 0.9\%$ and ΔPE is tiny while in the ASH-LBR equations $\Delta PE \approx 0.9\%$ and ΔE is tiny. In single-wave solutions ($\ell = 30$), the relative energy variations in the ASH-ANS equations are much larger ($\Delta E \approx 4.5\%$). Surprisingly, the solar atmosphere simulations show larger relative energy variations than similarly stratified isothermal atmosphere simulations, with ΔE being roughly five times larger in this solar atmosphere than in the corresponding $\Delta S/c_p = 0.4$ isothermal atmosphere. If we plotted these against $n_{\hat{\rho}}$, the solar simulations would lie midway between the $\Delta S/c_p = 0.1$ and 0.4 atmospheres and would still be clearly discrepant. We expect that the effects of energy non-conservation will become significantly larger as more entropy scale heights are included in the domain. This may be difficult to diagnose in simulations that include a realistic solar stratification as the radially varying Brunt-Väisälä frequency creates acoustic cavities that may trap high frequency gravity waves, but we expect that the low frequency waves which travel the entire radiative zone and experience the full stratification will be affected.

6. RECOMMENDATIONS FOR IMPROVING ANELASTIC TREATMENTS OF STELLAR INTERIORS

The results of Sections 3–5 provide a clear path to improving the treatment of dynamics within stably-stratified atmospheres in anelastic systems of equations. As clearly shown in Figure 5, the ANS equations do not conserve energy and instead conserve a stratification weighted pseudo-energy. These equations thereby obtain incorrect frequencies and radial eigenfunctions for gravity waves in both infinite and bounded isothermal atmospheres. The variation in the eigenfunctions is substantially larger than the level of energy non-conservation. These results hold in general for all subadiabatically-stratified atmospheres.

In contrast, the anelastic LBR equations do conserve energy and appear to need no additional modification to capture dynamics in subadiabatically-stratified regions. This is fairly surprising, as those equations are generally derived in nearly adiabatic atmospheres and the isothermal atmospheres we have considered here take them far from their realm of validity. At low vertical and horizontal wave numbers, eigenfunctions in the LBR equations differ from the full compressible equations, and results from gravity waves in this regime should be treated with caution. These differences shrink as either wavenumber increases and the LBR equations may do a reasonable job of capturing the dynamics of those shorter wavelength gravity waves (e.g., Figure 2). Though we did not explore their dynamics in direct numerical simulation, we

have demonstrated that the RG equations do not conserve energy in general atmospheres that have temperature gradients, and in those atmospheres will also likely obtain incorrect radial eigenfunctions.

To correctly capture the dynamics in sub-adiabatically stratified regions, it is vitally important that subsonic treatments of the fluid equations conserve energy. Systems of equations that conserve energy are physically self-consistent, even if simulations done with them have transport coefficients (e.g., ν and κ) that are several orders of magnitude larger than the molecular values in astrophysical systems. Systems that do not conserve energy are not physically consistent, and though the variations of energy may be small for some problems, these variations point to deeper underlying problems with those systems of equations. In particular, the eigenfunctions of the waves are significantly different in the non-conservative systems (e.g., ANS) from the energy conserving systems (e.g., FC and LBR), and this is very important for nonlinear transport, mode coupling and wave steepening and breaking. The clear path forward is to ensure that simulations employ anelastic systems of equations that conserve energy; fortunately this can be done with simple modifications to existing codes.

The route to energy conservation is to modify the momentum equation of the non-conservative systems. Fundamentally the conservation of energy is more physical than the conservation of momentum: there are many physical systems conserve energy instead of momentum, especially those where a very fast restoring force acts to constrain the behavior of the system. Examples of this include inelastic scattering off of rigid boundaries, where momentum changes sign but energy is conserved, and roller coasters on rigid tracks, where the track changes the momentum of the careening roller coaster but not its total energy. In anelastic systems, the fast sound waves provide the rapid restoring force and the divergence constraint embodied in equation (9) acts analogously to the rigid tracks of the roller coaster, applying a continuous forcing to the system. Fundamentally, this forcing is energy-conserving in the LBR equations but violates energy conservation in the ANS equations.

In simulation codes, there are two equivalent paths to convert the ANS equations into an energy conserving form identical to the LBR equations. The first path is by rewriting the equations to exactly match the anelastic LBR equations. This is done by solving for the reduced pressure ϖ instead of the fluctuating pressure P_1 , and by converting the buoyancy term to a ‘‘codensity’’ where entropy fluctuations S_1 contribute to buoyancy but pressure fluctuations do not. Doing so causes the momentum equation to take the following form

$$\frac{\partial \mathbf{u}}{\partial t} + \mathbf{u} \cdot \nabla \mathbf{u} = -\nabla \varpi - \frac{S_1}{c_p} \mathbf{g} - \nabla \cdot \mathcal{D}, \quad (127)$$

which is identical to the LBR momentum equation (110).

The second path to energy conservation is considerably simpler and relies on introducing a correction term into the momentum equation. Generally, energy non-conservation occurs in anelastic systems of equations when the reduced pressure ϖ interacts with the background stratification. The problematic term in the ANS momentum equation (18) is the $\varpi \nabla (S_0/c_p)$ term. We

modify the momentum equation to read

$$\frac{\partial \mathbf{u}}{\partial t} + \mathbf{u} \cdot \nabla \mathbf{u} = -\frac{1}{\rho_0} \nabla P_1 + \left(\frac{P_1}{\gamma P_0} + F_{\text{BVZ}} \right) \mathbf{g} - \frac{S_1}{c_p} \mathbf{g} - \nabla \cdot \mathcal{D}, \quad (128)$$

where the correction term is

$$F_{\text{BVZ}} = \frac{P_1}{g \rho_0} \nabla (S_0/c_p), \quad (129)$$

and where equation (128) reduces to the LBR momentum equation (110). We remind the reader that we have taken $\mathbf{g} = -g \hat{\mathbf{r}}$, and this sign is incorporated into equation (129). In a code like the ASH code, where the intermediate variable ρ_1 is carried around, this amounts to changing the equation of state for density fluctuations to

$$\frac{\rho_1}{\rho_0} = \frac{P_1}{\gamma P_0} + \frac{P_1}{g \rho_0} \nabla \left(\frac{S_0}{c_p} \right) - \frac{S_1}{c_p} = \frac{P_1}{g \rho_0} \nabla \ln \rho_0 - \frac{S_1}{c_p}. \quad (130)$$

Equations (127) and (128) are mathematically equivalent, but implementing this second path in a production code like ASH requires only a few lines of code and is considerably simpler than re-writing the equations in terms of ϖ . We have implemented both approaches in the ASH code, and the two paths to energy conservation give identical results in these test simulations.

The RG equations appear to not conserve energy in any atmosphere that has a temperature gradient. Instead they conserve a pseudo-energy weighted inversely by the background temperature T_0 in both stably-stratified radiative zones and in nearly adiabatically-stratified convection zones. This is an important distinction, as the differences between pseudo-energy conservation and energy conservation can appear in the RG equations even when $\Delta S/c_p$ is small. Instead, what matters is the number of temperature scale heights across the domain. This can be seen from the RG pseudo-density (103) and the associated pseudo-density scale height

$$n_{\hat{\rho}} = n_{\rho} - n_T, \quad (131)$$

where n_T is the number of temperature scale heights. (compare with eqn 113). In the RG equations, n_T has a similar but opposite role as $\Delta S/c_p$ in the ANS equations: increased n_T leads to less pseudo-density stratification. In the solar interior, T_0 is about $15 \times 10^6 \text{K}$ near the core, about $2 \times 10^6 \text{K}$ at the base of the convection zone ($0.7R_{\odot}$) and roughly $4 \times 10^5 \text{K}$ in the upper convection zone ($0.93R_{\odot}$). This leads to $n_T \approx 2$ and $n_{\hat{\rho}} \approx 4.7$ across the solar radiative zone ($0.001\text{--}0.7R_{\odot}$), and to $n_T \approx 1.6$ and $n_{\hat{\rho}} \approx 0.9$ across the deep convection zone ($0.7\text{--}0.93R_{\odot}$). The energy conserving properties of the RG equations could be studied in either a solar interior setting or in a polytropic atmosphere where there is a linear temperature gradient (e.g., Jones et al. 2011).

As with the ANS equations, it is straight-forward to put the RG equations into energy-conserving form. The term that leads to energy non-conservation is the $\varpi \nabla \ln T_0$ term in equation (26), which arises from a correction term,

$$\frac{1}{T_0} \frac{P_1}{g \rho_0} \frac{\partial T_0}{\partial r} g \hat{\mathbf{r}} = \varpi \nabla \ln T_0, \quad (132)$$

intended to more correctly capture sub-adiabatic stratifications (Rogers & Glatzmaier 2005b). If the RG mo-

mentum equation were re-written as

$$\frac{\partial \mathbf{u}}{\partial t} + \mathbf{u} \cdot \nabla \mathbf{u} = -\nabla \left(\frac{P_1}{\rho_0} \right) + \frac{T_1}{T_0} g \hat{\mathbf{r}}, \quad (133)$$

then these equations would conserve energy, though the frequencies of gravity waves in these equations remain a factor of $\sqrt{\gamma}$ higher than both the LBR frequencies and the low-frequency branch of the full compressible Euler equations. The source of this remaining disagreement remains unclear. It would be very interesting to see whether the non-conservation of energy has any impacts on the nature of convection in the RG equations, and on the coupling of convection to stably-stratified regions above and below.

Here we have explored how gravity waves in a solar radiative interior may be affected by anelastic treatments. The Boussinesq equations, which we have not considered here, are well known to conserve energy both linearly and nonlinearly, and this indicates that the issue is not the filtering of sound waves alone. Rather, it is the treatment of filtered, subsonic motions in a stratified atmosphere (in Boussinesq treatments the background density is constant). Other treatments of subsonic motions, such as the pseudo-incompressible equations and Reduced Sound Speed Techniques (e.g., Rempel 2005, 2006; Hotta et al. 2012) may similarly not conserve energy, and we would suggest that this be carefully tested. Generally, the isothermal atmospheres considered here or similar stably-stratified polytropic atmospheres (not considered here) provide simple test cases. The next paper in this series will consider variations on the pseudo-incompressible equations.

The subsonic dynamics of gravity waves may play an important role within the radiative envelopes in more massive stars, such as main-sequence A-, B- and O-type stars, where convective overshoot drives gravity waves up into a rarifying envelope leading to possible nonlinear wave breaking. Taking a CESAM model of a $2M_\odot$ A-type star, we estimate that the entropy change across the radiative envelope is about

$$(\Delta S/c_P)_{2M_\odot} = \int_{0.15R_*}^{0.97R_*} \frac{1}{c_P} \frac{\partial S_0}{\partial r} \approx 3.8, \quad (134)$$

which is substantially larger than the drop across the solar radiative zone (eq 126). Over this range of radii, $n_\rho \approx 16$ and $n_{\hat{\rho}} \approx 20$. Though we have focused on stellar interiors, energy conservation within anelastic systems is an important concern for dynamics in any stably-stratified atmosphere, including planetary atmospheres, planetary interiors, and astrophysical accretion disks (e.g., Barranco & Marcus 2005). Energy conservation in anelastic equations may also play an important role when magnetic fields are included in questions of the dynamics of magnetohydrodynamic instabilities including magnetic buoyancy instabilities (Berkoff et al. 2010).

Conservation of energy remains among the most sacrosanct and useful of principles in the physicist’s toolbox. The principle of energy conservation applies not only to ideal systems but furthermore to fundamentally dissipative or externally driven situations. In the latter scenarios, a time-dependent statement of energy budget replaces the simpler notion of time-constancy of total energy in an isolated ideal system. In all situations, we

believe that one should not tolerate the existence of uncontrolled spurious kinetic sources. For the particular problem of gravity and acoustic waves, this principle is more than philosophical. When examining the gravity and acoustic waves, energy-conserving anelastic models reproduce fully compressible results with much greater fidelity than energy-violating anelastic models; and this fact produces implications for our understanding of stellar interiors. Our particular work further shows that the existence of a conserved “pseudo-energy” does not rescue the energy non-conserving models. Rather, the existence of the pseudo-energy merely indicates why these problems appear to have gone unnoticed in previous simulations. However, including any nonlinear or dissipative effects leads to the impossibility of even proper pseudo-energy budgeting; in this case dissipation can even *inject* positive pseudo-energy. There is in short no way around the issue. Our best advice: properly account for energy whenever possible.

We thank Mark Miesch for his help in implementing the LBR equations in the ASH code (by more difficult path one). We thank Matthew Browning and Allan Sacha Brun for supplying the CESAM A-type star model. We thank Fausto Cattaneo for useful discussions about time-stepping errors. We thank Daniel Lecoanet, Mark Rast, Eliot Quataert and Gary Glatzmaier for reading this paper and making useful suggestions. We additionally thank Ann Almgren, Nic Brummell, Chris Jones, Jon Dursi, Keith Julien, Tami Rogers, Steve Tobias, Juri Toomre, Toby Wood and everyone previously thanked for useful discussions while exploring these anelastic equations. We thank the anonymous referee for their careful read of the paper. Ellen Zweibel thanks the Department of Astronomy at U. Chicago for their hospitality; a portion of this work was completed there. Benjamin Brown is supported in part by NSF Astronomy and Astrophysics postdoctoral fellowship AST 09-02004. CMSO is supported by NSF grant PHY 08-21899. The simulations were carried out with NSF PACI support of NICS and TACC.

APPENDIX

A. CONSERVATIVE FORM OF BUOYANCY TERM

When analyzing energy conservation properties in the anelastic equations (Section 4), the energy equation takes the general form

$$\frac{\partial K}{\partial t} + \nabla \cdot [\mathbf{u}(K + \rho_0 \varpi)] + \rho_0 \mathbf{u} \cdot \mathbf{g} \frac{S_1}{c_p} = RHS, \quad (A1)$$

with kinetic energy density $K = \rho_0 \mathbf{u}^2/2$ and where RHS is the right hand side (e.g., eqns 84 and 93). In equation (A1), the buoyancy work term takes the form $\rho_0 \mathbf{u} \cdot \mathbf{g} S_1$. We put this buoyancy work term into conservative form by using the gravitational potential, $\mathbf{g} = -\nabla \Phi$ and by recognizing the relation

$$\rho_0 \mathbf{u} \cdot \mathbf{g} S_1 = -\partial_t (\rho_0 \Phi S_1) - \nabla \cdot (\rho_0 \Phi \mathbf{u} S_1) - \Phi \rho_0 \mathbf{u} \cdot \nabla S_0. \quad (A2)$$

Using equation (A2), the left hand side (eqn. A1) can be put into conservative form

$$\frac{\partial E}{\partial t} + \nabla \cdot [\mathbf{u}(E + \rho_0 \hat{\varpi})] = RHS \quad (A3)$$

where

$$E = \rho_0 \left(\frac{|\mathbf{u}|^2}{2} - \Phi \frac{S_1}{c_p} \right), \quad (\text{A4})$$

$$\hat{\omega} = \varpi - \frac{1}{c_p} \int_a^r \Phi(r') dS_0(r'), \quad (\text{A5})$$

with a an arbitrary reference radius (here the radius of the lower boundary) and where the entropy profile is monotonic.

The energy defined in equation (A4) is slightly unusual in that the buoyancy contribution is not quadratic in entropy perturbation S_1 . This can be put in a more familiar quadratic form by first noting that for arbitrary (possibly nonlinear) motions

$$\rho_0 \mathbf{u} \cdot \mathbf{g} \frac{S_1}{c_p} = -\rho_0 \frac{d\Phi}{dS_0} \frac{S_1}{c_p} \mathbf{u} \cdot \nabla S_0 = \frac{\rho_0}{2c_p} \frac{d\Phi}{dS_0} \frac{DS_1^2}{Dt} = \partial_t A + \nabla \cdot (\mathbf{u} A) - A \mathbf{u} \cdot \nabla \ln \left(\frac{d\Phi}{dS_0} \right), \quad (\text{A6})$$

where the available potential energy A is given by

$$A = \frac{1}{2} \frac{\rho_0}{c_p} \frac{d\Phi}{dS_0} S_1^2, \quad (\text{A7})$$

and

$$\frac{d\Phi}{dS_0} = \frac{g(r)^2}{c_p N(r)^2}. \quad (\text{A8})$$

Equations (A6–A8) let us rewrite equation (A1) as

$$\frac{\partial \tilde{E}}{\partial t} + \nabla \cdot \left[\mathbf{u} (\tilde{E} + \rho_0 \hat{\omega}) \right] - A \mathbf{u} \cdot \nabla \ln \left(\frac{d\Phi}{dS_0} \right) = RHS, \quad (\text{A9})$$

where the alternative total energy \tilde{E} is

$$\tilde{E} \equiv \frac{1}{2} \rho_0 |\mathbf{u}|^2 + \frac{\rho_0}{2c_p} \frac{d\Phi}{dS_0} S_1^2, \quad (\text{A10})$$

and where $\hat{\omega}$ is given by equation (A5).

The left-hand side of equation (A9) can be put into conservative form if the condition

$$A \mathbf{u} \cdot \nabla \ln \left(\frac{d\Phi}{dS_0} \right) = 0 \quad (\text{A11})$$

is satisfied. This happens under two different conditions: (i) if $d\Phi/dS_0$ is constant, or (ii) we only consider linear perturbations. If condition (i) is satisfied (e.g., in isothermally- or adiabatically-stratified atmospheres) then equation (A11) holds for nonlinear motions as well and systems of equations with $RHS = 0$ will conserve a quadratic potential energy for nonlinear as well as linear motions.

B. EIGENFUNCTIONS FOR A BOUNDED ATMOSPHERE

Our analytic approach is similar to that in an infinite isothermal atmosphere, except now the wavelike perturbations are expanded in spherical harmonics and the radial eigenfunctions must be solved for. We take the spherical shell geometry of Section 5 and take impenetrable boundary conditions at the upper and lower boundary

$$\xi_r = 0 \text{ at } r = a, b \quad (\text{B1})$$

where $a = r_{\text{bot}}$ and $b = r_{\text{top}}$ (and see Table 4). Analytic eigenfunctions can be found if we consider a simplified atmosphere with constant gravity $\mathbf{g} = -g\hat{\mathbf{r}}$ and constant Brunt-Väisälä frequency N , and we do so here as well as in the main body of the text.

B.1. LBR eigenfunctions

We begin with the LBR equations. In this system, in a spherical shell geometry, equation (52) for reduced pressure ϖ becomes

$$\frac{\ell(\ell+1)}{r^2} \varpi = -\omega^2 \left[\xi_r H^{-1} - \frac{1}{r^2} \frac{\partial}{\partial r} (r^2 \xi_r) \right], \quad (\text{B2})$$

where we have used the anelastic continuity equation (9). Defining

$$\phi(r) \equiv \xi_r(r) r e^{(-r/2H)} \quad (\text{B3})$$

and

$$\lambda \equiv -\ell(\ell+1) (1 - N^2/\omega^2), \quad (\text{B4})$$

the momentum equation (60) becomes

$$-\frac{\partial}{\partial r} \left(r^2 \frac{\partial}{\partial r} \phi(r) \right) + \frac{r^2}{4H^2} \phi(r) = \lambda \phi(r). \quad (\text{B5})$$

For different λ the different $\phi(r)$ are orthogonal and this can be used to determine

$$\lambda = \frac{1}{4} + k^2, \quad (\text{B6})$$

where the vertical wavenumber k is normalized by the pressure and density scale height H . With equation (B4) we obtain the dispersion relationship

$$\omega^2 = \frac{\ell(\ell+1)}{\ell(\ell+1) + k^2 + \frac{1}{4}} N^2. \quad (\text{B7})$$

The vertical wavenumber k_n can be approximated as

$$k_n^2 = \frac{n^2 \pi^2}{\ln(\frac{b}{a})^2} \left(1 + \frac{b^2 - a^2}{8H^2} \frac{\ln(\frac{b}{a})}{n^2 \pi^2 + \ln(\frac{b}{a})^2} \right) + \mathcal{O}(H^{-4}) \quad (\text{B8})$$

for a spherical shell with lower boundary at $r = a$ and upper boundary at $r = b$. Exact solutions can be found numerically by solving the problem in terms of Bessel functions, with

$$\xi_{r,\text{LBR}}(r) = \left[K_{ik} \left(\frac{a}{2H} \right) I_{ik} \left(\frac{r}{2H} \right) - I_{ik} \left(\frac{a}{2H} \right) K_{ik} \left(\frac{r}{2H} \right) \right] r^{-3/2} \exp \left(\frac{r}{2H} \right), \quad (\text{B9})$$

where I_{ik} and K_{ik} are modified Bessel functions of the first and second kind respectively with imaginary index ik_n . The impenetrable boundary conditions at $r = b$ requires that $\xi(r) = 0$ and thus

$$K_{ik} \left(\frac{a}{2H} \right) I_{ik} \left(\frac{b}{2H} \right) - I_{ik} \left(\frac{a}{2H} \right) K_{ik} \left(\frac{b}{2H} \right) = 0, \quad (\text{B10})$$

which can be solved by Newton's method and using equation (B8) as an initial guess, yielding k_n .

B.2. ANS eigenfunctions

At this point the eigenfunctions for the linear ANS equations can be found by a simple transformation

$$\xi \rightarrow \xi \exp(-S_0/c_P), \quad (\text{B11})$$

$$H \rightarrow \gamma H, \quad (\text{B12})$$

which leads to

$$\varpi \rightarrow \varpi \exp(-S_0/c_P), \quad (\text{B13})$$

and transforms the linearized LBR wave equations (60) into the linearized ANS wave equations (51). This transformation leads to eigenfunctions of

$$\begin{aligned} \xi_{r,\text{ANS}}(r) = & \left[K_{ik} \left(\frac{a}{2\gamma H} \right) I_{ik} \left(\frac{r}{2\gamma H} \right) \right. \\ & \left. - I_{ik} \left(\frac{a}{2\gamma H} \right) K_{ik} \left(\frac{r}{2\gamma H} \right) \right] r^{-3/2} \exp \left((2\gamma - 1) \frac{r}{2\gamma H} \right). \end{aligned} \quad (\text{B14})$$

The vertical wavenumbers are found as before by solving

$$K_{ik} \left(\frac{a}{2\gamma H} \right) I_{ik} \left(\frac{b}{2\gamma H} \right) - I_{ik} \left(\frac{a}{2\gamma H} \right) K_{ik} \left(\frac{b}{2\gamma H} \right) = 0. \quad (\text{B15})$$

B.3. RG eigenfunctions

The linear RG are already in almost the same form as the LBR equations, except that

$$\lambda_{RG} \equiv -\ell(\ell + 1) (1 - \gamma N^2/\omega^2) = \frac{1}{4} + k^2. \quad (\text{B16})$$

Thus the solutions for radial wavenumber k and the radial eigenfunctions are the same as in the LBR equations, but the frequencies ω are a factor of $\sqrt{\gamma}$ higher than the Brunt-Väisälä frequency.

B.4. Normalization of eigenfunctions

As defined so far, the amplitude of the eigenfunctions ξ is a free parameter. In all sets of equations, we normalize the eigenfunctions by an amplitude A , with

$$A^2 = \frac{\int_a^b \xi(n, r)^2 \exp[-\epsilon r/H] r^2 dr}{\int_a^b \exp[-\epsilon r/H] r^2 dr}, \quad (\text{B17})$$

where ϵ represents the imaginary part of the vertical wavenumber K and is

$$\epsilon = \begin{cases} 2 - (1/\gamma) & \text{ANS equations} \\ 1 & \text{all others.} \end{cases} \quad (\text{B18})$$

This choice of normalization gives the correct amplitude for motions in the different systems of equations when subject to the same initial conditions (entropy perturbations of fixed initial amplitude); this is how we conduct the 3-D numerical simulations and thus the analytic eigenfunctions shown in Section 5.1 show the same amplitude ordering as the numerical simulations of Section 5.2.

REFERENCES

- Achatz, U., Klein, R., & Senf, F. 2010, *Journal of Fluid Mechanics*, 663, 120
 Almgren, A. S., Bell, J. B., Rendleman, C. A., & Zingale, M. 2006a, *ApJ*, 637, 922
 —. 2006b, *ApJ*, 649, 927
 Bannon, P. R. 1996, *Journal of Atmospheric Sciences*, 53, 3618
 Barranco, J. A. & Marcus, P. S. 2005, *ApJ*, 623, 1157
 Batchelor, G. K. 1953, *Quarterly Journal of the Royal Meteorological Society*, 79, 224
 Berkoff, N. A., Kersale, E., & Tobias, S. M. 2010, *Geophysical and Astrophysical Fluid Dynamics*, 104, 545
 Braginsky, S. I. & Roberts, P. H. 1995, *Geophysical and Astrophysical Fluid Dynamics*, 79, 1
 Brown, B. P., Browning, M. K., Brun, A. S., Miesch, M. S., & Toomre, J. 2008, *ApJ*, 689, 1354
 —. 2010, *ApJ*, 711, 424
 Brown, B. P., Miesch, M. S., Browning, M. K., Brun, A. S., & Toomre, J. 2011, *ApJ*, 731, 69:1
 Browning, M. K., Brun, A. S., & Toomre, J. 2004, *ApJ*, 601, 512
 Browning, M. K., Miesch, M. S., Brun, A. S., & Toomre, J. 2006, *ApJ*, 648, L157
 Brun, A. S., Antia, H. M., Chitre, S. M., & Zahn, J.-P. 2002, *A&A*, 391, 725
 Brun, A. S., Browning, M. K., & Toomre, J. 2005, *ApJ*, 629, 461
 Brun, A. S., Miesch, M. S., & Toomre, J. 2004, *ApJ*, 614, 1073
 —. 2011, *ApJ*, 742, 79
 Brun, A. S. & Toomre, J. 2002, *ApJ*, 570, 865
 Clune, T. L., Elliott, J. R., Glatzmaier, G. A., Miesch, M. S., & Toomre, J. 1999, *Parallel Computing*, 25, 361
 Drew, S. J., Jones, C. A., & Zhang, K. 1995, *Geophysical and Astrophysical Fluid Dynamics*, 80, 241
 Durran, D. R. 1989, *Journal of Atmospheric Sciences*, 46, 1453
 —. 2008, *Journal of Fluid Mechanics*, 601, 365
 Elliott, J. R., Miesch, M. S., & Toomre, J. 2000, *ApJ*, 533, 546
 Gilman, P. A. & Glatzmaier, G. A. 1981, *ApJS*, 45, 335
 Glatzmaier, G. A. 1984, *Journal of Computational Physics*, 55, 461
 —. 1985, *ApJ*, 291, 300
 Glatzmaier, G. A. & Roberts, P. H. 1996, *Science*, 274, 1887
 Gough, D. O. 1969, *Journal of Atmospheric Sciences*, 26, 448
 Hotta, H., Rempel, M., Yokoyama, T., Iida, Y., & Fan, Y. 2012, *A&A*, 539, A30
 Jones, C. A., Boronski, P., Brun, A. S., Glatzmaier, G. A., Gastine, T., Miesch, M. S., & Wicht, J. 2011, *Icarus*, 216, 120
 Jones, C. A. & Kuzanyan, K. M. 2009, *Icarus*, 204, 227
 Jones, C. A., Kuzanyan, K. M., & Mitchell, R. H. 2009, *Journal of Fluid Mechanics*, 634, 291
 Klein, R., Achatz, U., Bresch, D., Knio, O. M., & Smolarkiewicz, P. K. 2010, *Journal of Atmospheric Sciences*, 67, 3226
 Lantz, S. R. 1992, PhD thesis, CORNELL UNIVERSITY.
 Lantz, S. R. & Fan, Y. 1999, *ApJS*, 121, 247
 Lighthill, J. 1978, *Waves in fluids* (Cambridge University Press)
 Lipps, F. B. 1990, *Journal of Atmospheric Sciences*, 47, 1794
 Lipps, F. B. & Hemler, R. S. 1982, *Journal of Atmospheric Sciences*, 39, 2192
 —. 1985, *Journal of Atmospheric Sciences*, 42, 1960
 Miesch, M. S., Brun, A. S., DeRosa, M. L., & Toomre, J. 2008, *ApJ*, 673, 557
 Miesch, M. S., Elliott, J. R., Toomre, J., Clune, T. L., Glatzmaier, G. A., & Gilman, P. A. 2000, *ApJ*, 532, 593
 Mihalas, B. W. & Toomre, J. 1981, *ApJ*, 249, 349
 Nance, L. B. & Durran, D. R. 1994, *Journal of Atmospheric Sciences*, 51, 3549
 Nelson, N. J., Brown, B. P., Brun, A. S., Miesch, M. S., & Toomre, J. 2011, *ApJ*, 739, L38:1
 Nonaka, A., Almgren, A. S., Bell, J. B., Lijewski, M. J., Malone, C. M., & Zingale, M. 2010, *ApJS*, 188, 358
 Ogura, Y. & Phillips, N. A. 1962, *Journal of Atmospheric Sciences*, 19, 173
 Olson, P. & Christensen, U. R. 2006, *Earth and Planetary Science Letters*, 250, 561
 Rempel, M. 2005, *ApJ*, 622, 1320
 —. 2006, *ApJ*, 647, 662
 Roberts, P. H. & Glatzmaier, G. A. 2000, *Reviews of Modern Physics*, 72, 1081
 Rogers, T. M. & Glatzmaier, G. A. 2005a, *MNRAS*, 364, 1135
 —. 2005b, *ApJ*, 620, 432
 —. 2006, *ApJ*, 653, 756
 Rogers, T. M., Glatzmaier, G. A., & Jones, C. A. 2006, *ApJ*, 653, 765
 Rogers, T. M., Glatzmaier, G. A., & Woosley, S. E. 2003, *Phys. Rev. E*, 67, 026315
 Rogers, T. M. & MacGregor, K. B. 2010, *MNRAS*, 401, 191
 —. 2011, *MNRAS*, 410, 946
 Rogers, T. M., MacGregor, K. B., & Glatzmaier, G. A. 2008, *MNRAS*, 387, 616
 Zingale, M., Almgren, A. S., Bell, J. B., Nonaka, A., & Woosley, S. E. 2009, *ApJ*, 704, 196